

Stripped-envelope supernova light curves argue for central engine activity

Ósmar Rodríguez¹, Ehud Nakar^{1*} and Dan Maoz¹

¹School of Physics and Astronomy, Tel-Aviv University, Tel-Aviv,
Israel.

*Corresponding author(s). E-mail(s): udini@tauex.tau.ac.il;

Abstract

The luminosity of “stripped-envelope supernovae”, a common type of stellar explosions, has been generally thought to be driven by the radioactive decay of the nickel synthesized in the explosion and carried in its ejecta. Additional possible energy sources have been previously suggested[1–5], but these claims have been statistically inconclusive or model-dependent. Here, we analyse the energy budget of a sample of 54 well-observed stripped-envelope supernovae of all sub-types, and present statistically significant, largely model-independent, observational evidence for a non-radioactive power source in most of them (and possibly in all). We consider various energy sources, or alternatively, plausible systematic errors, that could drive this result, and conclude that the most likely option is the existence of a “central engine”, such as a magnetar (a highly magnetic neutron star) or an accreting neutron star or black hole, operating over hours to days after the explosion. We infer from the observations constraints on the engines, finding that if these are magnetars, then their initial magnetic fields are about 10^{15} G and their initial rotation period is 1–100 ms, implying that stripped-envelope supernovae could be the formative events of magnetars.

The light that we observe from supernovae (SNe) has several distinct energy sources. The two main ones are: the internal energy deposited in the envelope by the shock that unbinds the star, known as cooling-envelope emission; and the radioactive decay of ^{56}Ni that is synthesized during the explosion[6]. Two additional sources of energy are interaction of the ejecta with the circumstellar medium (CSM), and late energy injection by a central source – a “central engine”. Interaction with a CSM can typically

2 *Engines in stripped-envelope supernovae*

be identified by the presence of narrow lines in the SN spectrum. Central engines, however, are much harder to pin down.

Among the above energy sources, radioactive heating is considered to be the main one in SNe with compact stellar progenitors, such as the core-collapse of massive stars that have been stripped of most or all of their hydrogen envelopes at earlier stages of their stellar evolution—stripped-envelope (SE) SNe—which are sub-classified based on their spectra into types IIb, Ib, and Ic. Traditionally, a central engine has been invoked only in extremely energetic SNe, e.g. in some specific events[7–10], in luminous SNe[11], and in superluminous SNe[12–15]. However, the accepted view was that the power source of the light in most of the regular SE SNe, is completely dominated by radioactive decay. This view has been recently challenged. A method of analysis[16, 17], based on a development of the “Katz integral” approach[18], was used in a study[1] to estimate the ^{56}Ni mass (M_{Ni}) and the contribution of non- ^{56}Ni energy sources to the light curves of a sample of SNe of various types. The study found that, in the light curves of normal SE SNe, there are signs of an energy contribution from a source which cannot be ^{56}Ni , and which was attributed to cooling emission. However, the study assessed that this excess energy is comparable to the systematic errors, and therefore considered its detection tentative. A separate study[3] also found hints for a contribution from a non-radioactive source in SE SNe, based on a different approach. First, they measured M_{Ni} in a sample of such SNe, based on the luminosity in their radioactive tails. They then compared the luminosity of the peak in these SE SNe to the one predicted by numerical simulations, discovering that the observed peak luminosity is systematically brighter than the one predicted by simulations that are based on the measured values of M_{Ni} . A number of additional works, modeling the progenitors and their explosions, have also suggested that the amount of ^{56}Ni that can be synthesised during the explosion is insufficient to explain the peak luminosity of some observed SE SNe[2, 4, 5]. The indications of a non-radioactive source in all but the first (and statistically inconclusive) of these previous studies are, by nature, strongly model dependent.

We study a sample of 54 well-observed SE SNe ([Extended Data Fig. 1](#) and [Extended Data Table 1](#)) from among the 191 such events analyzed in a previous work[19]. The sample has bolometric light curves that are well-sampled over time, accurately measured ^{56}Ni masses (based on the radioactive tail luminosity), and relatively well constrained explosion times (see Methods for details). We use this sample to measure the contribution of non-radioactive power sources and to place constraints on the physical properties of such sources, utilizing and extending the Katz integral[18] method, to separate between the ^{56}Ni and non-radioactive contributions[16]. In the Methods section, we briefly repeat the derivation of the technique, and extend it to account for possible energy deposition by a central engine.

At times since explosion t , significantly longer than the diffusion time through the ejecta, t_{diff} , the extended Katz integral (equation (7) in Methods) can be written as

$$LT_{\text{-nuc}} \equiv LT(t) - QT_{\text{nuc}}(t) \approx ET + QT_{\text{eng}}(t) \quad ; \quad t \gg t_{\text{diff}}. \quad (1)$$

Here, $ET \equiv E(t_0) t_0$ is a constant, where $E(t)$ is the internal energy trapped in the ejecta as a function of time, and t_0 is the earliest time at which the expansion can

be regarded as homologous. $LT(t)$, $QT_{\text{nuc}}(t)$ and $QT_{\text{eng}}(t)$ are the time-weighted integrals from t_0 to t over the bolometric luminosity, $L(t)$, the energy deposition rate from radioactive decay, $Q_{\text{nuc}}(t)$, and the energy deposition rate from a central engine, $Q_{\text{eng}}(t)$, respectively (e.g. $LT(t) \equiv \int_{t_0}^t L(t') t' dt'$). Equation (1) separates the time-weighted integrated luminosity into the three possible energy sources that can power the emission (when there is no interaction with a CSM): the cooling emission ET , the radioactive decay QT_{nuc} , and the central engine QT_{eng} . We stress that equation (1) is quite robust and it is, basically, a kind of energy conservation statement that takes adiabatic losses into account. As such, it is independent of the uncertain radiative transfer in the problem as well as the velocity and abundances distribution of the ejecta. The only assumptions that underlie this equation are that the outflow is homologous and that the internal energy is dominated by radiation. Both of these assumptions are satisfied in all SNe that are not powered by interaction with a CSM, i.e., they are expected to be applicable to all normal SNe of types II, Iib, Ia, Ib, and Ic.

We have measured the above-defined excess over the radioactive heating contribution, $LT_{\text{-nuc}}$, and $LT_{\text{-nuc}}/LT_{100}$, for all of the SNe in our sample (Extended Data Table 3) where $LT_{100} \equiv LT(t = 100 \text{ d})$. Fig. 1 shows the cumulative distributions for the $LT_{\text{-nuc}}$ and $LT_{\text{-nuc}}/LT_{100}$ values. The most likely values of $LT_{\text{-nuc}}$ in our sample are all greater than zero. For all SNe, except four, $LT_{\text{-nuc}}$ is positive at $> 2\sigma$ significance. The mean $LT_{\text{-nuc}}$ values for the type-based subsamples of SNe Iib, Ib, and Ic are 2.4 ± 0.4 , 3.4 ± 0.4 , and $6.1 \pm 0.6 \times 10^{54} \text{ erg s}$ (errors are the standard error of the mean, SEM), respectively, which are at least 5.7 SEM greater than zero, while the average $LT_{\text{-nuc}}/LT_{100}$ value is 0.11 ± 0.01 , 0.13 ± 0.01 , and 0.21 ± 0.02 (± 1 SEM) for each SN type, respectively. In other words, $LT_{\text{-nuc}}$ is not only significantly greater than zero—it is also a sizeable fraction of LT_{100} . In Extended Data Fig. 1 we plot $L(t) \cdot t$ and $Q_{\text{nuc}}(t) \cdot t$ for each of the SNe in the sample. One sees that $L(t) \cdot t \approx Q_{\text{nuc}}(t) \cdot t$ is reached well before our somewhat-arbitrary choice of 100 days, and hence $LT_{\text{-nuc}}/LT_{100}$ provides a conservative estimate of the non-radioactive contribution to the peak of the light curve. Our results are consistent with those of the previous study[1] that found positive (but barely significant, as assessed by the authors) values of $LT_{\text{-nuc}}$ for 9 out of a sample of 11 SE SNe. Our results are more significant owing to our larger sample (54 versus 11 SNe), in which we have carefully considered all possible sources of errors (see Methods). We note that, in that previous study[1], the authors did not consider the possibility of a central engine, and therefore ET in their paper is equivalent to $LT_{\text{-nuc}}$.

The energy excess we measure in SE SNe is surprising, in view of the common wisdom that SE SNe, after the first day post-explosion, are powered solely by radioactive decay[20]. We therefore first consider the possibility that, rather than being physical, our result is an artifact of systematic errors. The observable $LT_{\text{-nuc}}/LT_{100}$ is independent of the adopted distances and bolometric-correction zero points, ruling out systematic errors in these parameters as driving the results (details of the derivation of L and M_{Ni} have been previously reported[19]). We have further considered the possibility of systematic errors in the adopted explosion time or the assumed dust reddening correction of each SN event, in the UV

and IR bolometric corrections, or in the assumption of isotropic emission, finding it highly unlikely that systematic errors in any of these can be the source of the positive values of LT_{nuc} (see Methods for details). We have also contemplated the effect of the adopted deposition function of the radioactive heat. For a theoretically plausible range of deposition functions, LT_{nuc} remains positive at high significance, while the LT_{nuc} values vary by tens of per cents between different deposition functions (see Methods). Thus, unless the deposition function is radically different than predicted by theory, its choice is not at the root of the positive values of LT_{nuc} . Moreover, many of the systematic errors would likely affect all of the SNe in our sample alike, regardless of their spectroscopic classification, but the different SN types display significantly different LT_{nuc}/LT_{100} distributions. Finally, we note the previous finding[1] that LT_{nuc} is consistent with zero for Type Ia SNe (as expected in the thermonuclear combustion of a white dwarf, which leaves no remnant), and therefore a systematic error in our method would somehow have to be restricted to SE SNe.

As the positive value of LT_{nuc} is most likely of physical origin, and there is no evidence for a CSM interaction in our SN sample (see Methods), the remaining possible excess energy sources are either cooling emission or a central engine. The cooling-emission option is arguably inconsistent with both theory and observations. First, if cooling emission dominates, then $ET \approx LT_{\text{nuc}} \sim 10^{54} - 10^{55}$ erg s. This implies that, for the SNe in our sample, the progenitor radius is $\sim 10^{13}$ cm, and that most of the ejecta mass is roughly at this radius before the explosion (i.e., this is not just the radius of some low-mass extended envelope; see Methods and ref.[21]). Such large pre-explosion radii run counter to stellar evolution models of SE SNe progenitors[22, 23]— see Methods for a discussion. Second, a large progenitor radius sets a lower limit on the bolometric luminosity at early times. However, for almost all of the SNe in our sample, the observed upper limit on L at these early times is below this minimum (see Methods). We conclude that the most likely explanation for the measured values of LT_{nuc} in our sample is the activity of a central engine.

If a central engine is the dominant energy source of LT_{nuc} , then we can constrain some of its properties. First, if all the injected energy thermalizes, then $E_{\text{eng}}t_{\text{eng}} \approx LT_{\text{nuc}}$ or, using fiducial numbers,

$$E_{\text{eng}} \approx 10^{49} \text{ erg} \left(\frac{t_{\text{eng}}}{10^5 \text{ s}} \right)^{-1} \frac{LT_{\text{nuc}}}{10^{54} \text{ erg s}}, \quad (2)$$

where, in the general case, E_{eng} is the energy deposited by the engine, and t_{eng} is the duration of this energy injection (see Methods of the exact definitions of E_{eng} and t_{eng} , and for a discussion of cases where they differ from the definitions above). If not all of the energy thermalizes, then equation (2) will be a lower limit on E_{eng} . From a combination of equation (2) with the requirement that the energy is deposited in time to affect the observations, we obtain the following constraints (see Methods

for details):

$$10^{48} - 10^{49} \text{ erg} < E_{\text{eng}} < 10^{51} - 10^{52} \text{ erg}, \quad (3)$$

$$10^3 - 10^4 \text{ s} < t_{\text{eng}} < 10^6 \text{ s}.$$

Long-lasting accretion onto the compact remnant is one possible source of the engine energy, although, it may be hard for such an engine to satisfy the above constraints (see Methods). A second option, which has been previously discussed in the context of SE SNe[24, 25], is a newly born magnetar. As we show here, it can naturally explain the observed $LT_{\text{-nuc}}$. A magnetar taps a stellar remnant's rotational energy and injects it into the ejecta via a magnetized wind. Requiring that the rotational energy and spin-down rate of the magnetar satisfy equations (2) and (3), we can constrain its magnetic field as follows (see Methods).

$$B \approx 10^{15} \text{ G} \left(\frac{LT_{\text{-nuc}}}{4 \times 10^{54} \text{ erg s}} \frac{\ln(t_{\text{peak}}/t_{\text{mag}})}{5} \right)^{-1/2}, \quad (4)$$

where B is the surface dipolar magnetic field, t_{mag} is the magnetar energy deposition time, and t_{peak} is the time where the observed luminosity peaks. The initial rotation period is constrained to the range $\sim 1 - 100$ ms (see Methods). These values for the magnetic field and the initial period align well with those expected for magnetars at birth.

SE SNe constitute $\sim 30\%$ of all core-collapse SN explosions[26], and so their roles are comparably important to other SN types in cosmic element synthesis and diffusion, in energy feedback in star and galaxy formation, in cosmic ray acceleration within old SN remnants, and potentially in the formation of the population of stellar-mass black holes. Our measurements and analysis suggest that in SE SNe there is a significant contribution to the observed luminosity, by post-explosion energy injection from a central object, on timescales of hours to days. If this central engine is a young, fast-spinning, magnetar, then its properties appear remarkably consistent with expectations for objects of this class at their formative phase. It has been estimated that 25–70% ($\pm 1 \sigma$ range) of neutron stars are born in SNe as magnetars[27], and hence our result is consistent with SE SNe being the main formation events of magnetars. Nonetheless, in other types of core-collapse SNe, the cooling emission phase is much more extended (~ 100 days, a result of the large progenitor radius), and therefore the Katz integral method is much less sensitive to the presence of central engines like those we have found here for SE SNe, and which would contribute in other SN types only of order a few per cent excess to the energy \times time budget. We therefore cannot exclude that other types of core-collapse SNe can perhaps also produce magnetars.

References

- [1] Sharon, A. & Kushnir, D. The γ -ray deposition histories of core-collapse supernovae. *Mon. Not. R. Astron. Soc.* **496** (4), 4517–4545 (2020).
- [2] Ertl, T., Woosley, S. E., Sukhbold, T. & Janka, H. T. The Explosion of Helium Stars Evolved with Mass Loss. *Astrophys. J.* **890** (1), 51 (2020).
- [3] Afsariardchi, N. et al. The Nickel Mass Distribution of Stripped-envelope Supernovae: Implications for Additional Power Sources. *Astrophys. J.* **918** (2), 89 (2021).
- [4] Woosley, S. E., Sukhbold, T. & Kasen, D. N. Model Light Curves for Type Ib and Ic Supernovae. *Astrophys. J.* **913** (2), 145 (2021).
- [5] Sollerman, J. et al. Maximum luminosities of normal stripped-envelope supernovae are brighter than explosion models allow. *Astron. Astrophys.* **657**, A64 (2022).
- [6] Woosley, S. E., Heger, A. & Weaver, T. A. The evolution and explosion of massive stars. *Reviews of Modern Physics* **74** (4), 1015–1071 (2002).
- [7] Maeda, K. et al. The Unique Type Ib Supernova 2005bf at Nebular Phases: A Possible Birth Event of a Strongly Magnetized Neutron Star. *Astrophys. J.* **666** (2), 1069–1082 (2007).
- [8] Wang, L. J. et al. Evidence for Magnetar Formation in Broad-lined Type Ic Supernovae 1998bw and 2002ap. *Astrophys. J.* **837** (2), 128 (2017).
- [9] Wang, L. J. et al. A Monte Carlo Approach to Magnetar-powered Transients. II. Broad-lined Type Ic Supernovae Not Associated with GRBs. *Astrophys. J.* **851** (1), 54 (2017).
- [10] Wang, S.-Q. et al. Modeling the Light Curves of the Luminous Type Ic Supernova 2007D. *Astrophys. J.* **877** (1), 20 (2019).
- [11] Gomez, S., Berger, E., Nicholl, M., Blanchard, P. K. & Hosseinzadeh, G. Luminous Supernovae: Unveiling a Population between Superluminous and Normal Core-collapse Supernovae. *Astrophys. J.* **941** (2), 107 (2022).
- [12] Inserra, C. et al. Super-luminous Type Ic Supernovae: Catching a Magnetar by the Tail. *Astrophys. J.* **770** (2), 128 (2013).
- [13] Nicholl, M., Guillochon, J. & Berger, E. The Magnetar Model for Type I Superluminous Supernovae. I. Bayesian Analysis of the Full Multicolor Light-curve Sample with MOSFiT. *Astrophys. J.* **850** (1), 55 (2017).
- [14] De Cia, A. et al. Light Curves of Hydrogen-poor Superluminous Supernovae

- from the Palomar Transient Factory. *Astrophys. J.* **860** (2), 100 (2018).
- [15] Lunnan, R. *et al.* Hydrogen-poor Superluminous Supernovae from the Pan-STARRS1 Medium Deep Survey. *Astrophys. J.* **852** (2), 81 (2018).
- [16] Nakar, E., Poznanski, D. & Katz, B. The Importance of ^{56}Ni in Shaping the Light Curves of Type II Supernovae. *Astrophys. J.* **823** (2), 127 (2016).
- [17] Wygoda, N., Elbaz, Y. & Katz, B. Type Ia supernovae have two physical width-luminosity relations and they favour sub-Chandrasekhar and direct collision models - I. Bolometric. *Mon. Not. R. Astron. Soc.* **484** (3), 3941–3950 (2019).
- [18] Katz, B., Kushnir, D. & Dong, S. An exact integral relation between the Ni56 mass and the bolometric light curve of a type Ia supernova. *arXiv e-prints arXiv:1301.6766*
- [19] Rodríguez, Ó., Maoz, D. & Nakar, E. The Iron Yield of Core-collapse Supernovae. *Astrophys. J.* **955** (1), 71 (2023).
- [20] Dessart, L. *et al.* Core-collapse explosions of Wolf-Rayet stars and the connection to Type IIb/Ib/Ic supernovae. *Mon. Not. R. Astron. Soc.* **414** (4), 2985–3005 (2011).
- [21] Shussman, T., Nakar, E., Waldman, R. & Katz, B. Type II supernovae progenitor and ejecta properties from the total emitted light, ET. *arXiv e-prints arXiv:1602.02774*
- [22] Yoon, S. C., Woosley, S. E. & Langer, N. Type Ib/c Supernovae in Binary Systems. I. Evolution and Properties of the Progenitor Stars. *Astrophys. J.* **725** (1), 940–954 (2010).
- [23] Laplace, E., Göteborg, Y., de Mink, S. E., Justham, S. & Farmer, R. The expansion of stripped-envelope stars: Consequences for supernovae and gravitational-wave progenitors. *Astron. Astrophys.* **637**, A6 (2020).
- [24] Woosley, S. E. Bright Supernovae from Magnetar Birth. *Astrophys. J.* **719** (2), L204–L207 (2010).
- [25] Kasen, D. & Bildsten, L. Supernova Light Curves Powered by Young Magnetars. *Astrophys. J.* **717** (1), 245–249 (2010).
- [26] Shivvers, I. *et al.* Revisiting the Lick Observatory Supernova Search Volume-limited Sample: Updated Classifications and Revised Stripped-envelope Supernova Fractions. *PASP* **129** (975), 054201 (2017).
- [27] Beniamini, P., Hotokezaka, K., van der Horst, A. & Kouveliotou, C. Formation rates and evolution histories of magnetars. *Mon. Not. R. Astron. Soc.* **487** (1), 1426–1438 (2019).

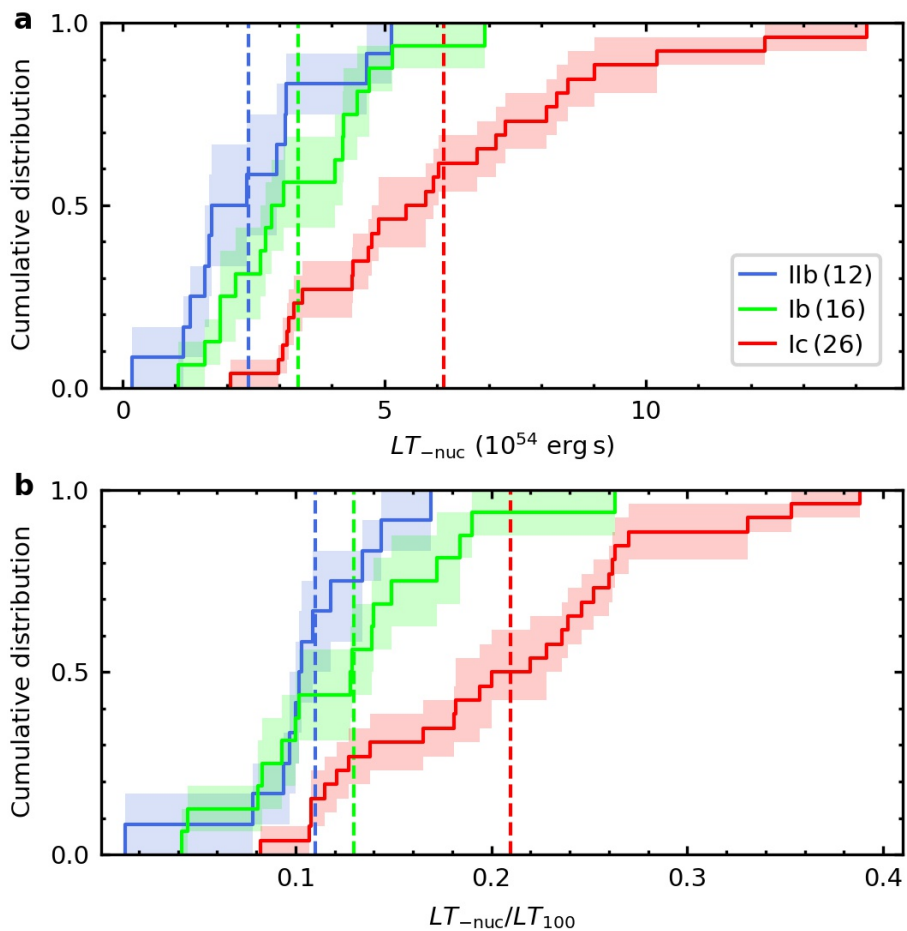


Fig. 1 The non-radioactive contribution to the light of SE SNe. Cumulative distributions for LT_{nuc} (a) and for LT_{nuc}/LT_{100} (b). Shaded regions represent 68% confidence intervals computed by bootstrap resampling (10,000 samples). Vertical dashed blue, green, and red lines indicate mean values for SNe IIb, Ib, and Ic, respectively. Numbers in parentheses are the sample sizes for each SE SN subtype.

Methods

The Katz Integral

We briefly repeat the derivation of the Katz integral[18] and its extension[16] to study energy sources beyond ^{56}Ni . In the Main Text, we further develop the separation of the ^{56}Ni and cooling-emission to take into account the contribution of a long lasting engine. Consider a non-relativistic, homologous, expanding outflow, with internal energy as a function of time since explosion, $E(t)$, dominated by the photons that are trapped in the ejecta. The derivative of this internal energy satisfies

$$dE(t)/dt = -E(t)/t + Q_{\text{dep}}(t) - L(t), \quad (5)$$

where the first term on the r.h.s accounts for the adiabatic losses of the trapped radiation, and the last term is the luminosity of the thermalized photons that escape the ejecta. $Q_{\text{dep}}(t)$ is the instantaneous energy deposition rate, in the form of thermalized photons, which in the absence of interaction of the ejecta with a CSM, has only two known possible sources—radioactive decay and the activity of a central engine:

$$Q_{\text{dep}} = Q_{\text{nuc}} + Q_{\text{eng}}. \quad (6)$$

Rearranging this derivative and integrating over the time, one obtains the Katz integral,

$$E(t)t - E(t_0)t_0 = \int_{t_0}^t (Q_{\text{dep}}(t') - L(t')) t' dt'. \quad (7)$$

The integration is from t_0 , the time at which homologous expansion begins, until any later time t . Since, by time t_0 , the radiation energy has become about an order of magnitude smaller than the total explosion energy, and the acceleration of the ejecta has become negligible, $E(t_0)$ is still completely dominated by the energy deposited by the shock that unbounds the stellar envelope, while the energy deposition by radioactive decay is not yet significant. When the time since explosion (which is also the dynamical time) becomes significantly longer than the diffusion time through the ejecta, t_{diff} , all of the energy that was trapped in the ejecta has escaped, and the term $E(t)t$ becomes comparable to $Q_{\text{dep}}(t) \cdot t_{\text{diff}}(t) \cdot t$, which vanishes with growing t .

Data Set

In a recent analysis[19], data were collected for 191 SE SNe from the literature and from the Zwicky Transient Facility (ZTF) Bright Transient Survey[28, 29], having known redshifts and photometry at peak light in at least two optical bands. For those SNe, the authors calculated distance moduli (μ), host galaxy reddenings ($E(B - V)_h$), explosion epochs (t_{exp}), and luminosities (L). To compute the luminosities, they used optical photometry (Johnson–Kron–Cousins $BVRI$, Sloan gr_i , and/or ZTF gr) and new bolometric corrections (BC), derived using 15 SNe I Ib, 15 SNe Ib, and 19 SNe Ic with optical and near-IR photometry from B to H/K (0.44 to 1.65/2.16 μm), including corrections to account for the unobserved flux at

wavelengths $< 0.44 \mu\text{m}$ and $> 1.65/2.16 \mu\text{m}$. From the luminosity light curves, they computed peak luminosities (L_{peak}), the corresponding peak times (t_{peak}), and decline rates defined as $\Delta m_{15} = 2.5 \log(L_{\text{peak}}/L(t_{\text{peak}} + 15 \text{d}))$. They further collected ejecta velocities at t_{peak} (v_{peak}), measured from absorption lines in optical spectra. For 75 SNe they computed M_{Ni} and gamma-ray escape times (t_{esc}) from the radioactive tail of their luminosity light curves, assuming a form[30] for the deposition function.

Among the 75 SE SNe with M_{Ni} estimates, we select for this work 54 SNe that have their first luminosity measurements at times $t_{\text{first}} \lesssim 10 \text{d}$ since explosion. Our final sample is listed in [Extended Data Table 1](#), which includes the SN name, the spectral subtype, μ , the heliocentric SN redshift z (throughout this work, all observed time intervals have been corrected by a factor $1 + z$ to bring them to the SN rest frame), the Galactic reddening[31] $E(B - V)_{\text{G}}$, $E(B - V)_{\text{h}}$, the absolute r -band magnitude at peak $M_{r,\text{peak}}$, the epochs of last non-detection $t_{\text{non-det}}$ and first SN detection t_{detect} , t_{exp} , and the filters of the photometry used by ref.[19] to compute luminosities through the BC technique. The luminosity light curves of the SNe in our sample, multiplied by the time since explosion, are shown in [Extended Data Fig. 1](#). [Extended Data Table 2](#) lists SN parameters, including M_{Ni} , t_{esc} , t_{peak} , L_{peak} , Δm_{15} , and v_{peak} .

Estimating $LT_{\text{-nuc}}$ from the observations

The observable $LT(t)$ can be expressed as

$$LT(t) = LT(t_{\text{first}}) + \int_{t_{\text{first}}}^t L(t') t' dt', \quad (8)$$

where $LT(t_{\text{first}}) = \int_0^{t_{\text{first}}} L(t') t' dt'$ is the contribution to $LT(t)$ from the unobserved luminosity at epochs earlier than t_{first} (the difference between integrating from $t = 0$ and integrating from $t = t_0$ is negligible). To estimate $LT(t_{\text{first}})$, we extrapolate the $(t_{\text{first}}, L(t_{\text{first}}))$ point linearly to zero luminosity at $t = 0$. Thus, $LT(t_{\text{first}})$ is equal to $L(t_{\text{first}}) t_{\text{first}}^2/3$, for which we assume a conservative relative error of 20%. The extrapolations of $L(t) t$ between the assumed explosion times and t_{first} are shown as red solid lines in [Extended Data Fig. 1](#).

For SE SNe in general, the dominant radioactive decay chain is $^{56}\text{Ni} \rightarrow ^{56}\text{Co} \rightarrow ^{56}\text{Fe}$, so

$$Q_{\text{nuc}}(t) = [q_{\gamma}(t) f_{\text{dep}}(t, t_{\text{esc}}) + q_{\text{pos}}(t)] M_{\text{Ni}}/M_{\odot}. \quad (9)$$

Here, $q_{\gamma}(t)$ and $q_{\text{pos}}(t)$ are the total energy release rates of gamma-rays and positron kinetic energy per unit M_{Ni} , respectively, while $f_{\text{dep}}(t, t_{\text{esc}})$ is the gamma-ray deposition function, which describes the fraction of the generated gamma-ray energy deposited in the ejecta. The terms $q_{\gamma}(t)$ and $q_{\text{pos}}(t)$ are given[17] by

$$q_{\gamma}(t) = \left(6.45 e^{-\frac{t}{\tau_{\text{Ni}}}} + 1.38 e^{-\frac{t}{\tau_{\text{Co}}}} \right) \times 10^{43} \text{ erg s}^{-1} \quad (10)$$

and

$$q_{\text{pos}}(t) = 0.046 \left(-e^{-\frac{t}{t_{\text{Ni}}}} + e^{-\frac{t}{t_{\text{Co}}}} \right) \times 10^{43} \text{ erg s}^{-1}, \quad (11)$$

where $t_{\text{Ni}} = 8.76$ days and $t_{\text{Co}} = 111.4$ days. We adopt the same gamma-ray deposition function[30] as in the data paper[19],

$$f_{\text{dep}}(t, t_{\text{esc}}) = 1 - e^{-(t_{\text{esc}}/t)^2}. \quad (12)$$

To compute $LT_{-\text{nuc}}$, the value of t in equation (1) must be much longer than the radiation diffusion time t_{diff} , such that $E(t)$ tends to zero and $L(t) \approx Q_{\text{nuc}}(t)$. Since at $t = t_{\text{peak}}$ the diffusion time is of the order of t_{peak} , while t_{diff} drops roughly as t^{-2} , we can assume $E(t) t = 0$ for $t \gtrsim 4 t_{\text{peak}}$. Given that the epoch of the last luminosity measurement (t_{last}) for the SNe in our sample are at least five times longer than t_{peak} , we adopt $t = t_{\text{last}}$ in equation (1). [Extended Data Fig. 1](#) shows, beside $L(t)$ t , the time-weighted radioactive energy deposition $Q_{\text{nuc}}(t) t$. The figure shows that in all the SNe in our sample $Q_{\text{nuc}}(t) t \approx L(t) t$ long before t_{last} , implying that the exact value of t_{last} has a negligible effect on the measurement of $LT_{-\text{nuc}}$. We calculate the integrals in $LT(t_{\text{last}})$ and $QT_{\text{nuc}}(t_{\text{last}})$ numerically using the trapezoidal rule.

The error on $LT_{-\text{nuc}}$, computed with error propagation, is given by

$$\sigma_{\log LT_{-\text{nuc}}} = \left[\frac{\sigma_{\mu}^2 + \sigma_{\text{BC}}^2 + \sigma_{\text{redd1,G}}^2 + \sigma_{\text{redd1,h}}^2}{6.25} + \frac{\sigma_{LT}^2 + \sigma_{QT}^2 + \sigma_{\text{exp1}}^2}{(LT_{-\text{nuc}} \ln 10)^2} \right]^{1/2}. \quad (13)$$

Here, the term σ_{BC} is the error due to uncertainties in the zero-points of the BC scales used in the data paper[19] to compute luminosities. The mean σ_{BC} values for SNe IIb, Ib, and Ic are 0.03, 0.04, and 0.05 mag, respectively. The terms $\sigma_{\text{redd1,G}}$ and $\sigma_{\text{redd1,h}}$ are the uncertainties due to errors in Galactic and host-galaxy reddenings, respectively, given by

$$\sigma_{\text{redd1,s}} = \left| \langle \zeta_s \rangle + (\langle \zeta_s \rangle - \langle \zeta_s \rangle^{\text{tail}}) \frac{QT_{\text{nuc}}(t_{\text{last}})}{LT_{-\text{nuc}}} \right| \sigma_{E(B-V)_s}, \quad (14)$$

with $s = \{\text{G}, \text{h}\}$. Here, ζ_s is defined as in the data paper[19], and depends on the extinction-to-reddening ratios of the optical bands used to compute luminosities through the BC technique, and on the dependence of BC on colour. $\langle \zeta_s \rangle$ is the average of the ζ_s values between t_{first} and t_{last} , while $\langle \zeta_s \rangle^{\text{tail}}$ is the mean of the ζ_s values in the radioactive tail. The typical $\langle \zeta_{\text{h}} \rangle$ ($\langle \zeta_{\text{h}} \rangle^{\text{tail}}$) values for SNe IIb, Ib, and Ic are 2.3 (2.1), 2.4 (2.2), and 3.3 (3.2), respectively, while the typical $\langle \zeta_{\text{G}} \rangle$ ($\langle \zeta_{\text{G}} \rangle^{\text{tail}}$) is of 2.7 (2.5). The term σ_{LT} is the uncertainty in $LT(t_{\text{last}})$ due to errors in luminosity, given by $\sigma_{LT} = (\sigma_{LT(t_{\text{first}})}^2 + \sigma_{LT,I}^2)^{1/2}$, where

$$\sigma_{LT,I} = \frac{1}{2} \left([(t_2 - t_1) t_1 \sigma_{L(t_1)}]^2 + \sum_{i=2}^{n-1} [(t_{i+1} - t_{i-1}) t_i \sigma_{L(t_i)}]^2 + [(t_n - t_{n-1}) t_n \sigma_{L(t_n)}]^2 \right)^{1/2} \quad (15)$$

is the error on the integral in equation (8), n being the number of data points in the luminosity light curve. The $L(t)$ errors do not include σ_μ , σ_{BC} , $\sigma_{E(B-V)_h}$, and $\sigma_{E(B-V)_G}$, which are already included in equation (13). The term σ_{QT} is the error in $QT_{\text{nuc}}(t_{\text{last}})$ due to uncertainties in $\log M_{\text{Ni}}$ and t_{esc} . To calculate σ_{QT} , we randomly select 10,000 pairs of $\log M_{\text{Ni}}$ and t_{esc} values from their posterior probability distribution, compute $QT_{\text{nuc}}(t_{\text{last}})$ using those values, and adopt the sample standard deviation of the 10,000 $QT_{\text{nuc}}(t_{\text{last}})$ estimates as σ_{QT} . In the data paper[19], we obtained this distribution for each SN by means of the Markov Chain Monte Carlo process implemented in the package EMCEE[32], which we used to compute $\log M_{\text{Ni}}$ and t_{esc} . The term σ_{texp1} in equation (13) is the error in $LT_{\text{-nuc}}$ due to the uncertainty in t_{exp} . Changes in t_{exp} not only affect t but also the values of $\log M_{\text{Ni}}$ and t_{esc} inferred from the radioactive tail of the luminosity light curves. To quantify variations in $LT_{\text{-nuc}}$ due to changes in t_{exp} , for each SN we compute $\log M_{\text{Ni}}$ and t_{esc} in the same manner as in the data paper[19] but using $t_{\text{non-det}}$ and t_{detect} to estimate the explosion time. These epochs correspond to the lowest and greatest possible value for t_{exp} , respectively. Then, we compute $LT_{\text{-nuc}}$ using $t_{\text{exp}} + \Delta t_{\text{exp}}$ as the explosion time, where Δt_{exp} is equal to $t_{\text{non-det}} - t_{\text{exp}}$ and $t_{\text{detect}} - t_{\text{exp}}$. Extended Data Fig. 2a shows the relative change in $LT_{\text{-nuc}}$ ($\Delta LT_{\text{-nuc}}/LT_{\text{-nuc}}$) against Δt_{exp} . The distribution, which is well represented by a straight line with intercept 0.002 and slope -0.067 d^{-1} , indicates that $LT_{\text{-nuc}}$ decreases as the time of explosion advances. Based on this, we adopt $\sigma_{\text{texp1}} = 0.067 |LT_{\text{-nuc}}| \sigma_{t_{\text{exp}}} \text{ d}^{-1}$.

The $LT_{\text{-nuc}}$ values and their errors are listed in Extended Data Table 3. The typical $\log LT_{\text{-nuc}}$ uncertainty is of 0.18 dex, corresponding to a relative $LT_{\text{-nuc}}$ error of 41%. On average, 71%, 12%, and 9% of the $LT_{\text{-nuc}}$ error is induced by uncertainties in $E(B-V)_h$, μ , and $QT_{\text{nuc}}(t_{\text{last}})$, respectively.

Estimating $LT_{\text{-nuc}}/LT_{100}$ from the observations

Given that host galaxy reddening and distance dominate the $LT_{\text{-nuc}}$ error budget, it is useful to compute $LT_{\text{-nuc}}/LT_{100}$, where $LT_{100} \equiv LT(t = 100 \text{ d})$. This ratio, which corresponds to the contribution of non-radioactive energy sources, $LT_{\text{-nuc}}$, to the time-weighted luminosity integrated over the first 100 days after explosion, is independent of the distance and of the zero-point of the BC scale, and less dependent on reddening than $LT_{\text{-nuc}}$. For 23 SNe in our sample with $t_{\text{last}} < 100 \text{ d}$, we compute LT_{100} using $LT_{100} = LT(t_{\text{last}}) + \int_{t_{\text{last}}}^{100 \text{ d}} Q_{\text{nuc}}(t) t dt$, assuming a conservative relative error of 20% for the integral.

The error in $LT_{\text{-nuc}}/LT_{100}$, computed with error propagation, is given by

$$\sigma_{LT_{\text{-nuc}}/LT_{100}} = \frac{LT_{\text{-nuc}}}{LT_{100}} \left[\sigma_{\text{redd2,G}}^2 + \sigma_{\text{redd2,h}}^2 + \frac{(\sigma_{LT}^2 + \sigma_{QT}^2)}{LT_{\text{-nuc}}^2} + \frac{\sigma_{LT_{100}}^2}{LT_{100}^2} + \frac{\sigma_{\text{texp2}}^2}{(LT_{\text{-nuc}}/LT_{100})^2} \right]^{1/2}, \quad (16)$$

where

$$\sigma_{\text{redd2},s} = \frac{\ln 10}{2.5} \left| (\langle \zeta_s \rangle - \langle \zeta_s \rangle_{\text{tail}}) \frac{QT_{\text{nuc}}(t_{\text{last}})}{LT_{\text{-nuc}}} \right| \sigma_{E(B-V)_s}, \quad (17)$$

$\sigma_{LT_{100}}$, similar to σ_{LT} , is the uncertainty in LT_{100} due to errors in luminosity, and $\sigma_{t_{\text{exp2}}}$ is the error in $LT_{\text{-nuc}}/LT_{100}$ due to uncertainties in t_{exp} . To quantify variations in $LT_{\text{-nuc}}/LT_{100}$ due to changes in t_{exp} , we proceed in the same manner as we did in the case of $LT_{\text{-nuc}}$. [Extended Data Fig. 2b](#) shows changes in $LT_{\text{-nuc}}/LT_{100}$ ($\Delta LT_{\text{-nuc}}/LT_{100}$) normalised to $LT_{\text{-nuc}}/LT_{100}$ against Δt_{exp} . The observed distribution, which is well represented by a straight line with intercept -0.003 and slope -0.047 d^{-1} , indicates that $LT_{\text{-nuc}}/LT_{100}$ decreases as the explosion epoch advances. Based on this, we adopt $\sigma_{t_{\text{exp2}}} = 0.047 |LT_{\text{-nuc}}/LT_{100}| \sigma_{t_{\text{exp}}} \text{ d}^{-1}$.

The $LT_{\text{-nuc}}/LT_{100}$ estimates and their errors are listed in [Extended Data Table 3](#). The mean $LT_{\text{-nuc}}/LT_{100}$ uncertainty is of 0.028, corresponding to a relative $LT_{\text{-nuc}}/LT_{100}$ error of 23%. On average, 42%, 31%, 13%, and 13% of the $LT_{\text{-nuc}}/LT_{100}$ error is induced by uncertainties in $QT_{\text{nuc}}(t_{\text{last}})$, $E(B-V)_h$, $LT(t_{\text{last}})$, and t_{exp} respectively.

Correlations

To investigate our results and to test for systematic errors that may artificially drive them, we have searched for correlations among the observables. [Extended Data Fig. 3](#) shows $LT_{\text{-nuc}}$ and $LT_{\text{-nuc}}/LT_{100}$ plotted against L_{peak} , M_{Ni} , t_{esc} , t_{peak} , v_{peak} , and Δm_{15} . For each of these pairs of variables, we compute Pearson's correlation coefficients (r) and the corresponding P values. We focus on strong ($|r| \geq 0.7$) and moderate ($0.5 \leq |r| < 0.7$) correlations with P values ≤ 0.05 , which are statistically significant at the $> 95\%$ level. For SNe I Ib, Ib, Ic, and SE SNe as a whole, we find a strong correlation between $LT_{\text{-nuc}}$ and L_{peak} (r values of 0.89, 0.70, 0.73, 0.79, respectively, and $P \leq 0.003$). For $LT_{\text{-nuc}}$ versus M_{Ni} , we find a strong correlation for SNe I Ib ($r = 0.82$, $P = 0.001$) and a moderate correlation for SNe Ic ($r = 0.50$, $P = 0.01$). The previously suggested[1] possible correlation between $LT_{\text{-nuc}}$ and t_{esc} is not reproduced in our analysis ($r = -0.06$, $P = 0.70$), and is likely a consequence of the small number (nine) of SE SNe used in that previous work. Indeed, using the $LT_{\text{-nuc}}$ and t_{esc} values of the eight SNe in common between the present work and the previous sample[1], we obtain $r = 0.78$ ($P = 0.02$), corresponding to a strong correlation. For SNe Ib we find a strong correlation between $LT_{\text{-nuc}}/LT_{100}$ and Δm_{15} ($r = 0.88$, $P < 0.001$) and a moderate correlation between $LT_{\text{-nuc}}/LT_{100}$ and M_{Ni} ($r = -0.53$, $P = 0.03$), while for SNe Ic we find moderate correlations between $LT_{\text{-nuc}}/LT_{100}$ and M_{Ni} , t_{peak} , and Δm_{15} (r values of -0.57 , -0.58 , and 0.69 , respectively, and $P \leq 0.002$). For SE SNe as a whole, we find moderate correlations between $LT_{\text{-nuc}}/LT_{100}$ and t_{peak} ($r = -0.63$, $P < 0.001$) and between $LT_{\text{-nuc}}/LT_{100}$ and Δm_{15} ($r = 0.63$, $P < 0.001$). Given that $LT_{\text{-nuc}}$ correlates with L_{peak} and that $LT_{100} = QT_{\text{nuc}}(t = 100 \text{ d}) + LT_{\text{-nuc}}$, where $QT_{\text{nuc}}(t = 100 \text{ d})$ is proportional to M_{Ni} , the quantity $LT_{\text{-nuc}}/LT_{100}$ is roughly proportional to $L_{\text{peak}}/M_{\text{Ni}}$. Therefore, the correlation between $LT_{\text{-nuc}}/LT_{100}$ and t_{peak} arises from the correlation between $L_{\text{peak}}/M_{\text{Ni}}$ and t_{peak} (known as the peak time-luminosity relation) that has been observed for SE SNe (e.g. see the data paper[19]),

while the correlation between $LT_{\text{-nuc}}/LT_{100}$ and Δm_{15} arises because $L_{\text{peak}}/M_{\text{Ni}}$ correlates not only with t_{peak} but also with Δm_{15} [19].

Selection bias

The selection criteria we have used to construct our SN sample are mainly connected to the temporal coverage of each SN light curve. This process could, in principle, somehow create a sample that is biased in its properties compared to the parent population of all SE SNe. To roughly evaluate the strength of any such bias, we compare our sample with the volume-limited (VL) samples used in the data paper[19]. These samples consist of 18 SNe Iib, 19 SNe Ib, and 29 SNe Ic with $\mu \leq 32.8, 33.3,$ and 34.0 mag, respectively, where the upper limits were selected such that the selection bias affecting the VL samples is relevant only for a small fraction of SNe with low luminosity. For the comparison, we use $M_{r,\text{peak}}$.

Extended Data Fig. 4 shows the cumulative distributions for the $M_{r,\text{peak}}$ values of the SNe Iib, Ib, and Ic in our sample and in the corresponding VL samples. To test, for each SN subtype, whether the $M_{r,\text{peak}}$ distribution for our sample and that for the VL sample are drawn from a common unspecified distribution (the null hypothesis), we use the two-sample Anderson-Darling test[33]. For each SN subtype we obtain Anderson-Darling P values greater than 0.38 (i.e., over the 0.05 critical level), meaning that the null hypothesis cannot be rejected. Assuming that the VL samples of the data paper[19] are adequate approximations for complete samples, then any selection bias affecting our SN sample is also not significant.

Robustness of the results

Our main result is that $LT_{\text{-nuc}}$ is significantly greater than zero and a non-negligible fraction of LT_{100} . As this result has far-reaching implications, it is important to consider possible unaccounted systematic errors that are responsible for it. To artificially obtain our result, we would need to systematically overestimate LT by 10–20% (depending on the SN type), and/or underestimate M_{Ni} by a similar amount. The fact that $LT_{\text{-nuc}}/LT_{100}$ is non-negligible for all SNe implies that our result is independent of the adopted distances and BC zero-points. Moreover, the systematic error should affect all the SNe in our sample, and be correlated with the SN type. We note also that, in a previous study[1], the authors found that $LT_{\text{-nuc}}$ is consistent with zero for SNe Ia, and therefore if there is a systematic error in our method it needs to be restricted to SE SNe. Below, we examine a number of possible errors, but find no error that is likely to explain our results.

Explosion time:

We first consider the effect of a systematic error in the estimated explosion time. Based on Extended Data Fig. 2 we find that later values of t_{exp} reduce $LT_{\text{-nuc}}$ and $LT_{\text{-nuc}}/LT_{100}$ while earlier values increase them. Thus, our $LT_{\text{-nuc}}$ and $LT_{\text{-nuc}}/LT_{100}$ estimates could be overestimated if the explosion epochs that we use are systematically too early. In the extreme case where $t_{\text{exp}} = t_{\text{detect}}$ (the latest possible value for t_{exp}), the mean $LT_{\text{-nuc}}/LT_{100}$ values for SNe Iib, Ib, and Ic reduce to

0.10 ± 0.01 , 0.11 ± 0.01 , and 0.19 ± 0.01 (1σ errors), respectively, which are only slightly lower than our original results and are still non-zero at high significance. Thus, our finding that SE SNe have non-zero $LT_{\text{-nuc}}$ values is not a result of the adopted explosion epochs.

Bolometric correction:

An additional source of error can be the bolometric correction (BC). Here, there are two possibilities. The first is that we have overestimated the luminosity around the peak, which leads to an overestimate of LT . We can check this by comparing our adopted luminosity to the integrated light in SNe with observations in all bands from the UV (based on *Neil Gehrels Swift Observatory* UVOT data) to the near-IR K band, which gives a lower limit on the luminosity. There are 10 SNe in our sample with such data, and in each of them the observed integrated light is $> 95\%$ of the peak luminosity that we have adopted. Thus, an overestimated BC near the peak is unlikely to explain the values of $LT_{\text{-nuc}}$.

A second option is an underestimate of the BC during the radioactive tail phase, that leads to an underestimate of M_{Ni} . For three SNe with *Swift* data during the tail we find that the contribution of the UV to the bolometric flux is less than 2%. Therefore, it is unlikely that there is a missing relevant contribution in the UV during the tail. To explore emission in the mid-infrared, we use SNe with *Spitzer* observations. There are only a handful of SE SNe with such observations during the first ~ 100 days, with the best studied case being SN 2011dh[34]. These SNe display mid-IR emission that, during the first 100 days after the peak, decreases with time more slowly than the emission in other bands. This slow drop has been attributed to emission by warm dust, and its fraction as part of the total luminosity grows slowly with time[35]. The heating source of this dust is probably radiative, either by the shock breakout or from the main SN emission, most likely near the peak. The time delay between this heating and the observed dust emission could be the result of light travel time. In any case, the light seen in the dust component at any given time of the light curve is a robust upper limit, and most likely results in a significant overestimate of the instantaneous emission that is lost to dust heating, and is therefore missing from our estimate of the bolometric luminosity. Mid-IR measurements are available for two of the SNe in our sample, 2011dh (Iib) and 2014L (Ic). A comparison of the dust luminosity (as estimated with a blackbody fit[34]) to the bolometric luminosity, for SN 2011dh, shows that the dust luminosity is about 1% of the total luminosity at day 17, and it is growing with time, reaching slightly less than 5% at day 84. A similar comparison for SN 2014L shows that the dust luminosity grows from 2.6% to 3.5% from day 40 to 67.

Our conclusion is that while dust absorption may have some effect on the estimated ^{56}Ni mass, this effect is small. It cannot be larger than a few per cent and most likely it is about 1% or less (at least in SN 2011dh and SN 2014L). This is certainly true if the dust optical depth is constant with time, and it is also true if the optical depth grows with time (e.g., due to dust formation), since a growing dust opacity mimics thermalization losses and therefore it is compensated, at least partially, by an underestimate of t_{esc} . Thus, it seems highly unlikely that systematic errors in the BC

are the source of the positive values of LT_{-nuc} that we find.

Host galaxy reddening:

The spectral energy distributions of SE SNe are bluer near maximum light than at later epochs (e.g. ref.[36]), so reddening corrections in the radioactive-tail phase will be lower than at epochs near peak. Overcorrecting for reddening can therefore produce a greater increment in LT than in QT_{nuc} , leading to an overestimated, and perhaps systematically non-zero, LT_{-nuc} .

Extended Data Fig. 5 shows LT_{-nuc} and LT_{-nuc}/LT_{100} against $E(B - V)_h$. We see that SNe with high values of LT_{-nuc} and LT_{-nuc}/LT_{100} do not necessarily have high $E(B - V)_h$ values. In addition, using only SNe with low host-galaxy reddening ($E(B - V)_h < 0.1$ mag), we obtain mean LT_{-nuc}/LT_{100} values of 0.09 ± 0.01 (7 SNe IIb), 0.13 ± 0.03 (7 SNe Ib), and 0.20 ± 0.02 (13 SNe Ic), values similar to those for the full sample, and still greater than zero at a high significance. Our non-zero LT_{-nuc} estimates are therefore not due to a systematic overestimate of the adopted host-galaxy reddening values.

Deposition function:

In this work we have adopted the deposition function[30] in equation (12) to describe the fraction of the generated gamma-ray energy deposited in the ejecta. Recently, a more versatile deposition function has been proposed[1], given by $f_{dep}^{S\&K} = (1 + (t/t_{esc})^n)^{-2/n}$, where n is an additional free parameter that controls the sharpness of the transition between the gamma-ray optically thick and thin regimes. The ^{56}Ni masses calculated with this deposition function are, on average, 14% larger than those computed assuming equation (12)[19]. Since larger ^{56}Ni masses produce larger QT_{nuc} values, our LT_{-nuc} and LT_{-nuc}/LT_{100} estimates could be overestimated if $f_{dep}^{S\&K}$ is the true deposition function for SE SNe.

Extended Data Fig. 6a shows LT_{-nuc} calculated assuming $f_{dep}^{S\&K}$ as the deposition function ($LT_{-nuc}^{S\&K}$) against the LT_{-nuc} estimates reported in this work. For the 24 SE SNe with reasonable n values ($n > 1$; see ref.[1]) shown in the figure, we see that the $LT_{-nuc}^{S\&K}$ values are mostly lower than our LT_{-nuc} estimates but still greater than zero. Extended Data Fig. 6b shows the cumulative distribution for the ratio of $LT_{-nuc}^{S\&K}$ to our LT_{-nuc} estimates. The mean $LT_{-nuc}^{S\&K}/LT_{-nuc}$ values are 0.78 ± 0.10 (6 SNe IIb), 0.62 ± 0.10 (3 SNe Ib), and 0.71 ± 0.06 (15 SNe Ic), which are statistically consistent with each other. Therefore, if $f_{dep}^{S\&K}$ is the true deposition function for SE SNe, then our LT_{-nuc} and LT_{-nuc}/LT_{100} estimates are overestimated, on average, by a factor of 1.4. In particular, the mean LT_{-nuc}/LT_{100} values reduces to 0.09 ± 0.01 , 0.08 ± 0.01 , and 0.15 ± 0.02 for SNe IIb, Ib, and Ic, respectively, which are still significantly greater than zero. Thus, it seems unlikely that our non-zero LT_{-nuc} estimates result from our adopted deposition function. Yet, given the sensitivity of the exact value of LT_{-nuc} and LT_{-nuc}/LT_{100} to the adopted deposition function, in the unlikely case that the deposition in reality is very different than the forms suggested by theory, it may be the source of the positive values of LT_{-nuc} .

Asphericity:

Equation (1) is independent of the geometry of the ejecta. However, our estimates of L and M_{Ni} from the observations do assume spherical symmetry, and a deviation from spherical symmetry could lead to an over- or underestimate of both L and M_{Ni} . The errors in the estimates of L and M_{Ni} are not necessarily the same and this may introduce a non-zero value of LT_{nuc} . However, as explained below, for some SNe asphericity could potentially increase the value of LT_{nuc} , but then for a similar number of SNe it would then reduce its value. The fact that all SNe show a positive value of LT_{nuc} implies that asphericity is not a dominant systematic effect.

If the SN emission is not isotropic then, since we assume that L is proportional to the observed flux, some observers will infer a peak luminosity that is higher than the actual one, while others will infer a luminosity that is lower. The same will happen during the radioactive tail phase, with observers who measure higher values of L during peak, also measuring a higher value of M_{Ni} . However, since the optical depth of the entire ejecta drops with time, the emission becomes more isotropic. Thus, the over- and underestimates of M_{Ni} are closer to the true (direction-averaged) values than the over- and underestimate of L , and thus of LT , near peak time. The result is that even if radioactive decay were the only energy source, an observer who overestimates LT by some factor is expected to overestimate M_{Ni} by a lower factor and thus to measure a positive LT_{nuc} . An observer of the same SN from a different viewing angle, who underestimates LT by some factor will underestimate M_{Ni} by a lower factor and hence will measure a negative LT_{nuc} . As in our sample there is not a single SN with a negative value of LT_{nuc} , it is unlikely that that the entire effect we measure results from asphericity, when in fact LT_{nuc} is zero.

Interaction with a circumstellar medium

CSM interaction is an efficient source of energy for SN emission. The emission from CSM interaction depends strongly on the optical depth of the medium. If the medium is optically thin for absorption then the emission is nonthermal, extending from radio to X-rays. If it is optically thick to absorption, then it can peak in the UV/optical/IR. However, in that case, during the time that the interaction takes place the transfer of the radiation through the unshocked CSM generates narrow emission lines, which are the hallmark of CSM interaction.

Observations of normal SE SNe, such as those that constitute our sample, strongly disfavor the possibility that interaction contributes a significant fraction of the UV/optical/IR emission seen in most or all such SNe. This is supported by three independent lines of evidence:

- a) Many normal SE SNe, including some of the SNe in our sample, are accompanied by synchrotron radio emission that arises from CSM interaction[37]. This emission arises from interaction of the fastest moving ejecta, at velocities of $30,000 \text{ km s}^{-1}$ and more, with an optically thin wind. The contribution of this emission to the SN UV/optical/IR light is completely negligible. There are no signs in radio or X-ray for an additional interaction that could contribute to the UV/optical/IR emission.
- b) As explained above, a significant contribution of CSM interaction to the UV/optical/IR light, without displaying bright emission in the radio and/or X-rays, requires

interaction with an optically thick medium. However, in that case narrow lines are expected, but which are observed in none of the SNe in our sample.

c) During CSM interaction, the radiation is generated at the leading edge of the ejecta (where the interaction takes place) and the arrival time of photons to the observer is determined by the diffusion time through the unshocked CSM. There is no reason to expect that the time of the peak of this emission coincides with the peak of the radioactive emission, which is determined by the diffusion time through the entire ejecta. The fact that in all SNe in our sample there is a single peak in the light curve, which coincides with the expected contribution of radioactive power, argues that CSM interaction is not a dominant source of light, at least in the majority of these SNe. Note that the above considerations are distinct from those related to the time at which engine-powered emission is released. The reason is that, unlike CSM interaction, the engine deposits its energy at the base of the ejecta and (assuming energy deposition before the peak) this energy is released together with the peak of the radioactive powered emission, i.e. when the diffusion time through the ejecta is comparable to the expansion time. Our conclusion is that CSM interaction cannot be the source of $LT_{\text{-nuc}}$, at least in most (and most likely all) of the SNe in our sample.

Progenitor radius assuming that $ET \approx LT_{\text{-nuc}}$

If the main energy source of $LT_{\text{-nuc}}$ is cooling emission, then we can estimate the progenitor radius (or more specifically an integral over its pre-explosion mass density distribution[21]). The value of ET is determined by the progenitor properties and the explosion energy. This has been discussed in detail[21], and it was shown that $ET = A(E_{\text{exp}}M_{\text{ej}})^{1/2}R_{\text{prog}}$, where E_{exp} is the total explosion energy, M_{ej} is the ejecta mass, R_{prog} is the progenitor radius, and A is a proportionality coefficient that depends on the exact density distribution of the pre-explosion progenitor and on deviations from spherical symmetry. This relation can be understood as follows. Each fluid element reaches its homologous expansion phase roughly when it arrives at double the radius at which it was shocked. Its internal energy at this time is proportional to its kinetic energy (where the latter dominates the former by up to an order of magnitude). For the bulk of the progenitor mass, the internal energy is proportional to E_{exp} , and the time at which it becomes homologous is roughly $R_{\text{prog}}/(E_{\text{exp}}/M_{\text{ej}})^{1/2}$, so $ET \equiv E(t_0)t_0 \propto E_{\text{exp}}R_{\text{prog}}/(E_{\text{exp}}/M_{\text{ej}})^{1/2} = (E_{\text{exp}}M_{\text{ej}})^{1/2}R_{\text{prog}}$.

The value of A reflects the distribution of mass within the progenitor and the deviations of the explosion from spherical symmetry, if there are any. Progenitors with mass that is concentrated toward the core will have a smaller A values, compared to a progenitor with mass that is spread out closer to the surface. It was found that for a large range of red supergiant progenitors calculated with the stellar-evolution code MESA[38], the average A value is 0.15[21]. Carrying out a similar calculation for analytic profiles of stars with radiative envelopes (as expected for SE SNe progenitors), where the mass distribution is slightly more concentrated than in stars with convective envelopes, we find $A \approx 0.1$. We can therefore estimate the radius of the progenitor with the following relation:

$$LT_{\text{-nuc}} \approx ET \approx 0.1(E_{\text{exp}}M_{\text{ej}})^{1/2}R_{\text{prog}}$$

$$= 3 \times 10^{52} \text{ erg s} \left(\frac{E_{\text{exp}}}{10^{51} \text{ erg}} \frac{M_{\text{ej}}}{5 M_{\odot}} \right)^{\frac{1}{2}} \frac{R_{\text{prog}}}{10^{11} \text{ cm}}. \quad (18)$$

Note that R_{prog} is not necessarily the photospheric radius of the star, but rather the radius where most of the mass is concentrated (see discussion below).

In order to evaluate R_{prog} in the case that $ET = LT_{\text{-nuc}}$, we use a rough estimate of M_{ej} and E_{exp} from the observables: $M_{\text{ej}} \approx (\beta/2)\kappa^{-1}c t_{\text{peak}}^2 v_{\text{peak}}$ and $E_{\text{exp}} \approx 0.3 M_{\text{ej}} v_{\text{peak}}^2$, where β is an integration coefficient that depends (among other things) on the ejecta density and velocity distributions, κ is an effective opacity and c is the speed of light. Here we use, following precedent[39], $\beta = 13.7$ and $\kappa = 0.07 \text{ cm}^2 \text{ g}^{-1}$. Plugging these relation into equation (18) we obtain

$$\begin{aligned} R_{\text{prog}} &\sim \frac{LT_{\text{-nuc}}}{5c t_{\text{peak}}^2 v_{\text{peak}}^2} \\ &\approx 10^{13} \text{ cm} \frac{LT_{\text{-nuc}}}{3 \times 10^{54} \text{ erg s}} \left(\frac{t_{\text{peak}}}{15 \text{ d}} \frac{v_{\text{peak}}}{10^4 \text{ km s}^{-1}} \right)^{-2}. \end{aligned} \quad (19)$$

Given that the approximations of the explosion energy and the ejecta mass are crude, we assess the accuracy of this relation at about an order of magnitude. Applying equation (19) to the SNe in our sample, we find that, if the non-radioactive energy source is dominated by cooling emission, then the progenitors have radii in the range

$$R_{\text{prog}} \sim 5 \times 10^{12} - 5 \times 10^{13} \text{ cm}. \quad (20)$$

We re-emphasize that R_{prog} is the radius where most of the ejecta resides before the explosion, rather than the photospheric radius. Thus, in progenitors that have a low-mass extended envelope, R_{prog} is the core radius, which can be smaller than the photospheric radius by orders of magnitude. As discussed below, this distinction is especially important in the context of SE SNe, since some of their progenitors, especially of type IIb, have such a low-mass extended envelope.

Stellar evolution models of SE SNe progenitors[22, 23] predict the following structures. If the star retains a non-negligible hydrogen envelope ($\sim 0.01 - 0.1 M_{\odot}$), then this envelope expands to hundreds of solar radii, while the helium core retains a radius of $\sim 10^{11} \text{ cm}$. Such progenitors are expected to produce Type IIb SNe. If hydrogen is removed below some mass threshold then helium is abundant in the envelope and the envelope radius depends on its core mass. For a core mass larger than about $3 M_{\odot}$, the envelope is compact and the photospheric radius is at most a few solar radii. For core mass lower than about $3 M_{\odot}$ the envelope expands to $\sim 100 R_{\odot}$ and the progenitor becomes a helium giant. However, similar to the case above of progenitors with a low-mass hydrogen envelope, here too the extended envelope contains only a small fraction of the mass while over 95% of the stellar mass is confined to no more than a few solar radii[22]. Thus, since R_{prog} , which dominates the contribution to ET , reflects the radius of the core, we conclude that the constraints found in equation (19) are inconsistent with stellar-evolution models of SE SN progenitors.

Observationally, in almost all cases of SE SNe in which progenitor candidate stars have been identified in pre-explosion images, the SN was of type IIb. These are SNe that have retained a small amount of hydrogen, and therefore the expectation is that the progenitor has a massive core, surrounded by a low-mass envelope. This expectation is supported by the observations. The observational signature of such a progenitor is a pre-explosion photospheric radius of a supergiant, and a double-peaked SN light curve, where the first peak is due to shock cooling and the second is dominated by ^{56}Ni [40]. Well known examples are the Type IIb SNe 1993J and 2011dh. Pre-explosion images found that they had supergiant progenitors with photospheric radii of about 10^{13} cm[41, 42]. The cooling emission of the envelope in these SNe peaked within a few days of the explosion, indicating that the measured radius of each progenitor represents the photosphere of a low-mass hydrogen envelope ($\lesssim 0.1 M_{\odot}$), while most of the ejecta mass originated from a much more compact core[43, 44], even if the radius of this core is not tightly bound by observations. In the single unambiguous case of a pre-explosion detection of a Type Ib SN progenitor, the estimated pre-explosion radius is $\sim 3 \times 10^{12}$ cm, and here too the theoretical models suggest that the progenitor had a massive core with a low-mass extended envelope[45]. We conclude that the observations support the stellar evolution models, according to which the value we measure for LT_{nuc} cannot be dominated by cooling envelope emission. Nonetheless, as the observations do not provide direct constraints on the core radii of the progenitors, we cannot completely rule out this possibility.

Fortunately, the bolometric light curves of the SNe themselves allow us to carry out a direct observational consistency test of the hypothesis that $LT_{\text{nuc}} = ET$. If there were no ^{56}Ni in the ejecta (and no engine) then all of the emission would be cooling emission. In such a case, the luminosity would be very high during shock breakout ($\sim 10^{44}$ erg s $^{-1}$). Then, during the ensuing cooling emission phase, after a short episode of a rapid decay, the luminosity would start decaying slowly, roughly as $t^{-0.35}$ [46]. This phase of shallow decay stops once the photosphere's location is affected by recombination, at which point the luminosity evolution flattens even further (or even rises very slowly), roughly to a plateau with a luminosity L_{plat} . The plateau ends at time t_{plat} with an abrupt drop, as the diffusion time through the entire ejecta becomes comparable to the dynamical time (i.e. the time since explosion). This behaviour of the predicted light curve of a ^{56}Ni -free SE SN can be seen in numerical models[20]. When observed, it implies that, with no ^{56}Ni and no engine, $ET = LT_{\text{nuc}} = LT \approx L_{\text{plat}}t_{\text{plat}}^2/2$. When the ejecta does contain ^{56}Ni , the early light curve remains unchanged, as the cooling emission dominates over the radioactive power. The ^{56}Ni power starts affecting the emission only about one day, or even a few days, after the explosion, the exact time depending on the degree of ^{56}Ni mixing in the external layers of the ejecta, and on the progenitor radius. Thus, as long as the cooling emission dominates the luminosity, the light curve decays or remains roughly constant with time. Once the ^{56}Ni power begins to dominate, the luminosity increases with time up to the main peak a few weeks past explosion. This behaviour of the light curve (including a direct comparison between SE SNe light curve with and without ^{56}Ni) can be seen in numerical simulations[20], and a detailed discussion[47] of the

early light curve from ^{56}Ni -powered SNe exists as well. From that discussion we see that, at any time before the peak of a SN that contains ^{56}Ni , the luminosity L is larger than, or at most comparable to, the cooling emission of a similar SN that does not contain any ^{56}Ni , i.e. $L \gtrsim L_{\text{plat}}$ for any $t < t_p$. An additional effect of the ^{56}Ni power is that it raises the temperature of the ejecta, compared to the ^{56}Ni -free case, and therefore recombination is delayed. This results in higher optical depth of the ejecta and therefore $t_p \geq t_{\text{plat}}$ (this effect is again seen in the numerical simulations[20]).

From the discussion above, and as we show below, we can use the observed light curves to set a robust upper limit on the value of $L_{\text{plat}}t_{\text{plat}}^2/2$ in the SNe in our sample (under the hypothetical assumption that they would not have contained any ^{56}Ni) and thus on ET in that case. However, since ET is independent of the amount of ^{56}Ni in the ejecta, this upper limit on ET is also applicable to the contribution of cooling envelope emission to the actual light curves in our sample, which are dominated by ^{56}Ni power. To set this upper limit, we use the fact that, at any time, the light curve of a SN with ^{56}Ni is comparable to, or brighter than, the light curve of the same explosion without ^{56}Ni , i.e. at all times the observed $L(t) \geq L_{\text{plat}}$. We therefore can treat the luminosity of the faintest data point observed before the peak in the light curve of each SNe, denoted L_{min} , as an upper limit on L_{plat} . We note that the true value if L_{plat} in most cases is likely much lower than L_{min} . We know this because, in most SNe in our sample, L_{min} is set by the first detection and, at that time, the light curve is already rising sharply, implying that L_{min} is most likely already dominated by ^{56}Ni power at that stage. Taking this upper limit together with $t_p \geq t_{\text{plat}}$, we obtain $L(t)t_{\text{peak}}^2/2 \geq L_{\text{plat}}t_{\text{plat}}^2/2 \approx ET$. Thus, if $LT_{\text{-nuc}}$ in our sample is dominated by cooling emission, it must satisfy $LT_{\text{-nuc}} \lesssim L_{\text{min}}t_{\text{peak}}^2/2$.

Applying this test to our sample, we find that 90% of the SNe have $LT_{\text{-nuc}}$ values greater than $L_{\text{min}}t_{\text{peak}}^2/2$. For 19% of the sample we even obtain $LT_{\text{-nuc}}$ values 5 times greater than $L_{\text{min}}t_{\text{peak}}^2/2$. These results imply that cooling emission from the explosion of a large-radius progenitor is an unlikely explanation for our excess $LT_{\text{-nuc}}$ result.

Constraints on the central engine properties

Here we consider the constraint on the properties of a central engine that contributes $QT_{\text{eng}} \approx 10^{54} - 10^{55}$ erg s to the light curve of a SE SN. We consider an engine with energy injection rise time that is shorter than its operation time and that, after its power injection peaks, its luminosity as well as $d \log(Q_{\text{eng}})/d \log(t)$ decline roughly monotonically. The engine can show rapid variability on timescales that are much shorter than its operation time, in which case Q_{eng} can be considered as the average energy injection over the variability time. The two main engine candidates, an accreting central compact object and a rapidly rotating magnetar, both satisfy these assumptions. Under these assumptions, $QT_{\text{eng}}(t) \sim Q_{\text{eng}}(t)t^2$ as long as $d \log(Q_{\text{eng}})/d \log(t) > -2$. Thus, defining t_{eng} such that $d \log(Q_{\text{eng}})/d \log(t)|_{t=t_{\text{eng}}} = -2$, the value of QT_{eng} at late times satisfies $QT_{\text{eng}}(t > t_{\text{eng}}) \approx Q_{\text{eng}}(t_{\text{eng}})t_{\text{eng}}^2$. We define $E_{\text{eng}} \approx Q_{\text{eng}}t_{\text{eng}}$ as the energy injected over time scale t_{eng} . In the general case, E_{eng} is the total energy deposited

by the engine and t_{eng} is the duration of this energy injection. However, this is not the case for all types of engine temporal evolution. If there is an extended phase during which $-2 < d \log(Q_{\text{eng}})/d \log(t) < -1$, then the total energy injected by the engine (over a time scale much shorter than t_{eng}) can be significantly larger than E_{eng} .

The engine energy cannot be larger than the total explosion energy, therefore $E_{\text{eng}} < E_{\text{exp}}$, where $E_{\text{exp}} \sim 10^{51} - 10^{52}$ erg. In addition, since the value of LT_{nuc} is dominated by the emission during the peak, the engine energy injection must take place before or during the peak of the emission, $t_{\text{eng}} \lesssim t_{\text{peak}}$, where in our sample $t_{\text{peak}} \sim 10^6$ s. These upper limits together with equation (2) and our finding that $LT_{\text{nuc}} \approx 10^{54} - 10^{55}$ erg s in our sample, lead to the constraints given in equation (3).

To conclude, the engine should inject its energy over a duration that is longer than about an hour and shorter than about a week, where the shorter time scale corresponds to an injected energy of $\sim 10^{51} - 10^{52}$ erg and the longer one corresponds to $\sim 10^{48} - 10^{49}$ erg. Next we discuss the two main candidates for central engines, accretion and a fast spinning magnetar.

Accretion onto a compact remnant

In principle, the energy released during accretion of in-falling material onto a newly formed neutron star or black hole can provide more than enough energy to power the non-radioactive emission. Equation (2) implies an accreted mass of

$$M_{\text{acc}} \approx 10^{-4} M_{\odot} \left(\frac{\epsilon_{\text{acc}}}{0.1} \right)^{-1} \left(\frac{t_{\text{acc}}}{10^5 \text{ s}} \right)^{-1} \frac{LT_{\text{nuc}}}{10^{54} \text{ erg s}}, \quad (21)$$

where t_{acc} is the accretion time and ϵ_{acc} is the efficiency at which energy is extracted from the accretion. This is a reasonable amount of mass in the aftermath of a core collapse. The corresponding accretion rate is

$$\dot{M}_{\text{acc}} \approx 10^{-9} M_{\odot} \text{ s}^{-1} \left(\frac{\epsilon_{\text{acc}}}{0.1} \right)^{-1} \left(\frac{t_{\text{acc}}}{10^5 \text{ s}} \right)^{-2} \frac{LT_{\text{nuc}}}{10^{54} \text{ erg s}}, \quad (22)$$

a hyper-Eddington rate. It is much too low for efficient cooling by neutrinos, yet much higher than the $\sim 10^{-16} M_{\odot} \text{ s}^{-1}$ Eddington accretion rate for a disk that cools via photons.

The required accretion timescale is hard to explain naturally, where the main difficulty is how to sustain accretion for longer than 10^3 s after the ejection of the envelope. During the SN explosion $10^{51} - 10^{52}$ erg are deposited in the envelope. This energy unbinds the entire envelope within at most a few hundred seconds. Note that this is true even if the energy deposition is highly aspherical[48]. Thus, the naive expectation (see alternative option below) is that the accretion disk should form within this time, and therefore the duration of accretion that lasts for more than 10^3 s is most likely dominated by the accretion time of the disk, t_{acc} . This time can be estimated using an effective dimensionless viscosity parameter α , where $t_{\text{acc}} \sim \alpha^{-1} T_{\text{orb}}/2\pi \sim 300 \text{ s} (\alpha/0.01)^{-1} (M_{\text{rem}}/M_{\odot})^{1/2} (r_{\text{disk}}/10^9 \text{ cm})^{3/2}$, M_{rem} is

the compact remnant mass, T_{orb} is the orbital time of the disk, and r_{disk} is its radius. Note that we assumed here a thick disk, as expected for the highly hyper-Eddington accretion rates needed to power such an engine. Yet another constraint is on the free-fall time of the material that forms the disk, which should be shorter than the time at which the deposited energy unbinds the envelope, namely a few hundred seconds. This maximal free-fall time implies that the material that forms the disk must originate from an initial radius of no more than about 10^{10} cm in the progenitor.

We conclude that, for a typical accretion scenario, the simple limits that we derive here allow for an accretion-powered engine, although not in a very natural way. The disk in this scenario should form at a radius of $\sim 10^9 - 10^{10}$ cm, outside the radius of the pre-collapsed core. The mass from the disk should free-fall from an initial radius $\lesssim 10^{10}$ cm, implying a fast-rotating progenitor (so that the specific angular momentum of the pre-explosion envelope fits a Keplerian orbit of the formed disk). Finally, such accretion can power only an engine with a duration that is consistent with the lower-limit of equation (3) ($10^3 - 10^4$ s).

An alternative accretion model is one where the SN shock unbinds almost the entire envelope, and sends a minute fraction of the stellar mass (of order of M_{acc}) to marginally bound trajectories. In such a case, the fallback of M_{acc} onto the compact remnant can last as long as needed to power the engine. Testing this model is extremely difficult, as it is challenging to follow numerically the hydrodynamics of such a small fraction of the ejecta mass.

Magnetar properties

If the engine is a magnetar, then we can further constrain its magnetic field and initial rotation. The energy that can be contributed by a magnetar is its rotational energy, $E_{\text{mag}} \approx 2 \times 10^{52} \text{ erg } P_i^{-2}$ where $P_i = P_{i,\text{ms}} \cdot 1 \text{ ms}$ is its initial rotation period. Dividing this energy by the spin-down luminosity [49], one obtains the time over which this energy is injected into the ejecta, $t_{\text{mag}} \approx 10^3 \text{ s } P_{i,\text{ms}}^2 B_{15}^{-2}$ where $B = B_{15} \times 10^{15} \text{ G}$ is the surface dipolar magnetic field. The luminosity of the magnetar wind is roughly constant over t_{mag} , so its value is about $E_{\text{mag}}/t_{\text{mag}}$ during this time. At $t > t_{\text{mag}}$ the luminosity drops as t^{-2} , so under the assumption that the entire wind energy thermalizes, $QT_{\text{eng}}(t)$ increases logarithmically at $t > t_{\text{mag}}$, and therefore $QT_{\text{eng}}(t > t_{\text{mag}}) \approx E_{\text{mag}} t_{\text{mag}} \ln(t/t_{\text{mag}})$. Thus, requiring $QT_{\text{eng}}(t > t_{\text{peak}}) \approx LT_{\text{nuc}}$, we obtain the constraints on the magnetar dipolar magnetic field (equation 4) and on the initial spin period.

Acknowledgements. We thank Amir Sharon, Doron Kushnir and Avishai Gilkis for comments and discussions. This work was supported by grants No. 818899 (E.N.) and 833031 (D.M.) from the European Research Council (ERC).

Author Contributions. O.R. and E.N. conceived the idea to measure the Katz integral for these data. O.R. performed the data analysis, revealing the excess power source. E.N. led the theoretical analysis of the nature of the excess. All three authors took part in the discussions, analysis, and writing of the manuscript. Correspondence and requests for materials should be addressed to O.R. and/or E.N.

Competing interests. The authors declare no competing interests.

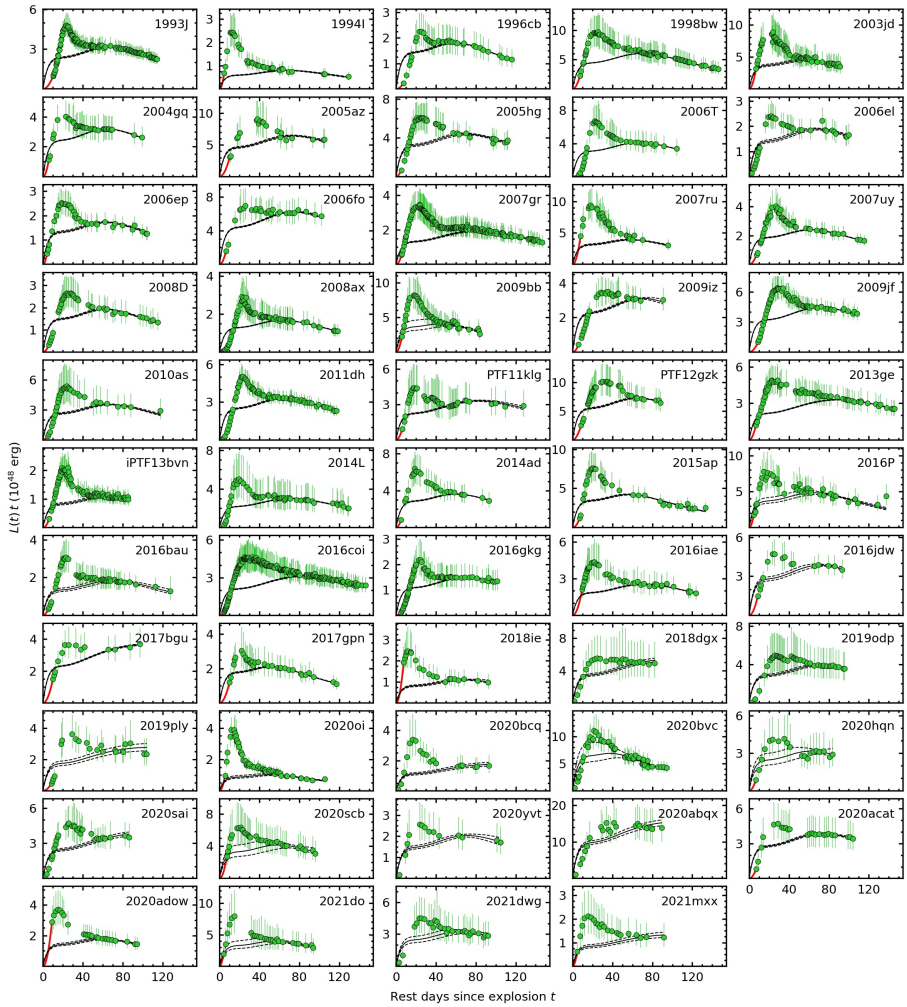
Data availability. The data used to create the figures in this study, as well as the scripts used to generate the figures, are available online in Zenodo with the identifier

Code availability. We used Python 3.7.6 and the public Python packages NumPy 1.19.4 and Matplotlib 3.4.1. The stellar-evolution code MESA is freely available and documented at <https://docs.mesastar.org/en/release-r23.05.1/>.

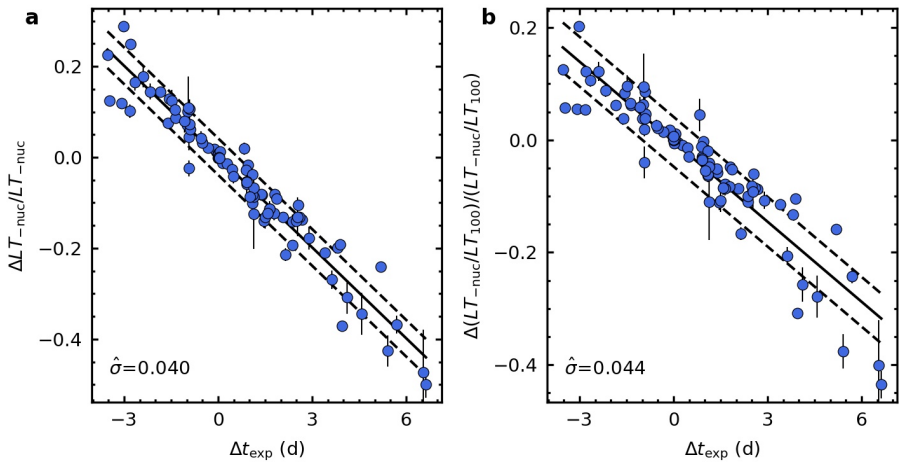
References

- [28] Fremling, C. *et al.* The Zwicky Transient Facility Bright Transient Survey. I. Spectroscopic Classification and the Redshift Completeness of Local Galaxy Catalogs. *Astrophys. J.* **895** (1), 32 (2020).
- [29] Perley, D. A. *et al.* The Zwicky Transient Facility Bright Transient Survey. II. A Public Statistical Sample for Exploring Supernova Demographics. *Astrophys. J.* **904** (1), 35 (2020).
- [30] Clocchiatti, A. & Wheeler, J. C. On the Light Curves of Stripped-Envelope Supernovae. *Astrophys. J.* **491** (1), 375–380 (1997).
- [31] Schlafly, E. F. & Finkbeiner, D. P. Measuring Reddening with Sloan Digital Sky Survey Stellar Spectra and Recalibrating SFD. *Astrophys. J.* **737** (2), 103 (2011).
- [32] Foreman-Mackey, D., Hogg, D. W., Lang, D. & Goodman, J. emcee: The MCMC Hammer. *PASP* **125** (925), 306 (2013).
- [33] Scholz, F. W. & Stephens, M. A. K-Sample Anderson–Darling Tests. *Journal of the American Statistical Association* **82** (399), 918–924 (1987).
- [34] Tinyanont, S. *et al.* A Systematic Study of Mid-infrared Emission from Core-collapse Supernovae with SPIRITS. *Astrophys. J.* **833** (2), 231 (2016).
- [35] Szalai, T., Zsíros, S., Fox, O. D., Pejcha, O. & Müller, T. A Comprehensive Analysis of Spitzer Supernovae. *Astrophys. J. Supp.* **241** (2), 38 (2019).
- [36] Stritzinger, M. D. *et al.* The Carnegie Supernova Project I. Methods to estimate host-galaxy reddening of stripped-envelope supernovae. *Astron. Astrophys.* **609**, A135 (2018).
- [37] Chevalier, R. A. Synchrotron Self-Absorption in Radio Supernovae. *Astrophys. J.* **499** (2), 810–819 (1998).
- [38] Paxton, B. *et al.* Modules for Experiments in Stellar Astrophysics (MESA). *Astrophys. J. Supp.* **192** (1), 3 (2011).
- [39] Prentice, S. J. *et al.* Investigating the properties of stripped-envelope supernovae; what are the implications for their progenitors?

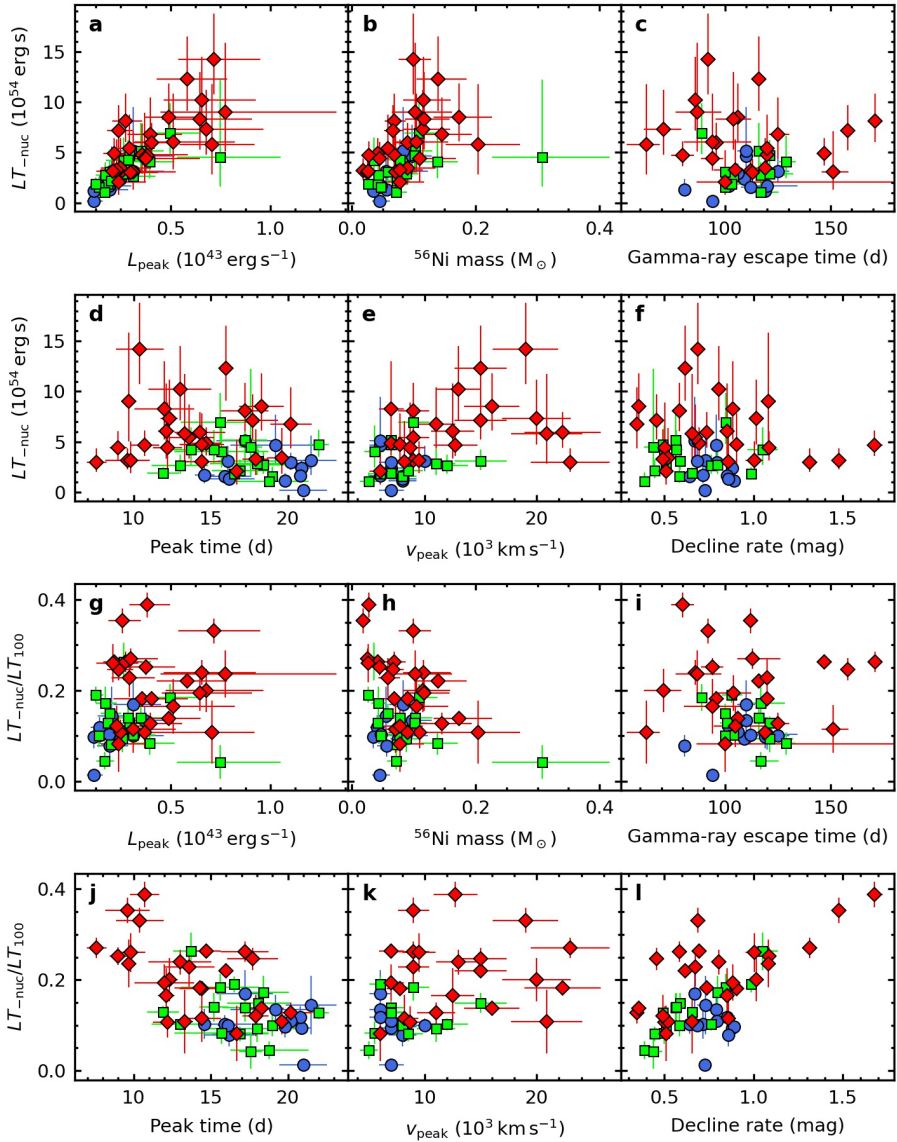
- Mon. Not. R. Astron. Soc. **485** (2), 1559–1578 (2019).
- [40] Nakar, E. & Piro, A. L. Supernovae with Two Peaks in the Optical Light Curve and the Signature of Progenitors with Low-mass Extended Envelopes. Astrophys. J. **788** (2), 193 (2014).
- [41] Aldering, G., Humphreys, R. M. & Richmond, M. SN 1993J: The Optical Properties of its Progenitor. Astron. J. **107**, 662 (1994).
- [42] Van Dyk, S. D. et al. The Progenitor of Supernova 2011dh has Vanished. Astrophys. J. **772** (2), L32 (2013).
- [43] Blinnikov, S. I., Eastman, R., Bartunov, O. S., Popolitov, V. A. & Woosley, S. E. A Comparative Modeling of Supernova 1993J. Astrophys. J. **496** (1), 454–472 (1998).
- [44] Bersten, M. C. et al. The Type IIb Supernova 2011dh from a Supergiant Progenitor. Astrophys. J. **757** (1), 31 (2012).
- [45] Gilkis, A. & Arcavi, I. How much hydrogen is in Type Ib and IIb supernova progenitors? Mon. Not. R. Astron. Soc. **511** (1), 691–712 (2022).
- [46] Nakar, E. & Sari, R. Early Supernovae Light Curves Following the Shock Breakout. Astrophys. J. **725** (1), 904–921 (2010).
- [47] Piro, A. L. & Nakar, E. What can we Learn from the Rising Light Curves of Radioactively Powered Supernovae? Astrophys. J. **769** (1), 67 (2013).
- [48] Eisenberg, M., Gottlieb, O. & Nakar, E. Observational signatures of stellar explosions driven by relativistic jets. Mon. Not. R. Astron. Soc. **517** (1), 582–596 (2022).
- [49] Spitkovsky, A. Time-dependent Force-free Pulsar Magnetospheres: Axisymmetric and Oblique Rotators. Astrophys. J. **648** (1), L51–L54 (2006).



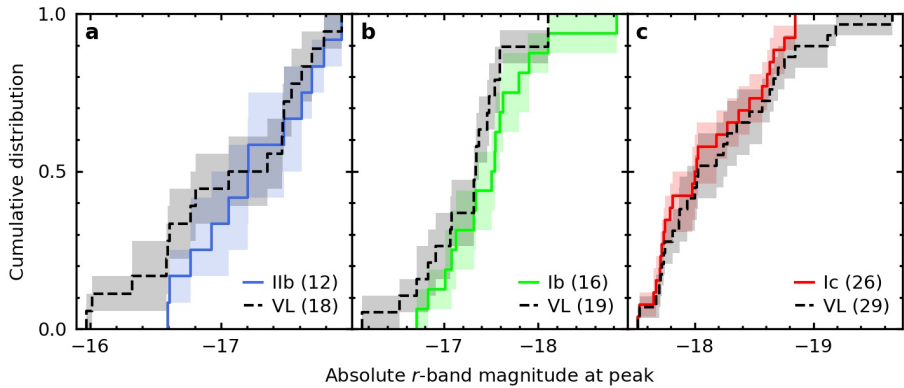
Extended Data Fig. 1 Time-weighted luminosity light curves for the SNe in our sample. Red solid lines are extrapolations of $L(t)$ t to $t = 0$. Black solid lines are time-weighted energy injection due to the radioactive decay chain $^{56}\text{Ni} \rightarrow ^{56}\text{Co} \rightarrow ^{56}\text{Fe}$, while dashed lines correspond to the 5th–95th percentile error range due to uncertainties in M_{Ni} and t_{esc} . Error bars are 1σ and include propagated uncertainties in distance, reddening, bolometric correction, and photometry.



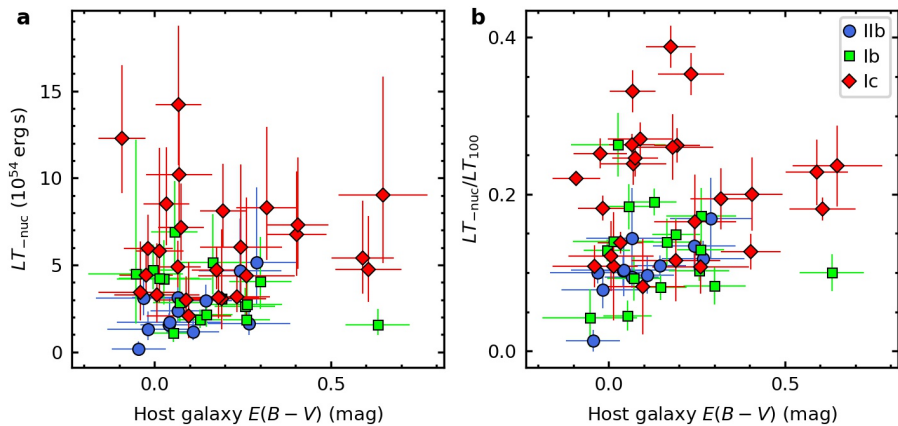
Extended Data Fig. 2 The effect of change in the estimated explosion time. Relative change in LT_{nuc} (a) and LT_{nuc}/LT_{100} (b) against change in explosion time. Negative (positive) Δt_{exp} values are quantities computed using $t_{\text{non-det}}$ (t_{detect}) as explosion time. Error bars are 1σ . Solid lines are straight line fits and dashed lines are $\pm 1\hat{\sigma}$ limits, where $\hat{\sigma}$ is the sample standard deviation.



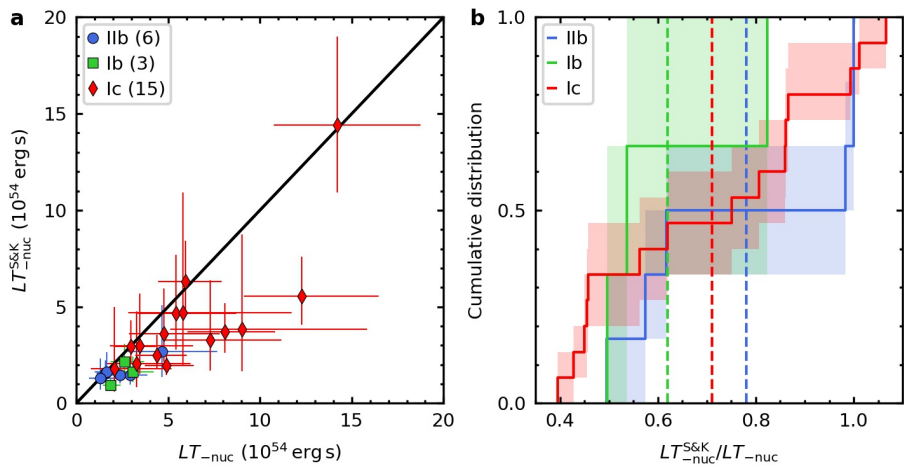
Extended Data Fig. 3 Correlations between the non-radioactive contribution and various quantities. LT_{nuc} (a–f) and LT_{nuc}/LT_{100} (g–l) against peak luminosity (a, g), ^{56}Ni mass (b, h), gamma-ray escape time (c, i), peak time (d, j), ejecta velocity at peak time (e, k), and decline rate (f, l). Error bars here and in subsequent figures denote 1σ errors.



Extended Data Fig. 4 Peak luminosity comparison of our sample to a volume-limited sample. Cumulative distributions for the absolute r -band magnitudes at peak of the SNe IIb (a), Ib (b), and Ic (c) in our sample (solid lines) and in the volume-limited samples of ref.[19] (dashed lines). Shaded regions represent 68% confidence intervals computed by bootstrap resampling (10,000 samples). Numbers in parentheses are the sample sizes.



Extended Data Fig. 5 The effect of extinction. LT_{nuc} (a) and LT_{nuc}/LT_{100} (b) against host galaxy reddening.



Extended Data Fig. 6 The effect of the radioactive energy deposition function. **a.** LT_{nuc} computed with the deposition function of Sharon & Kushnir against the LT_{nuc} estimates reported in this work. The solid line is a one-to-one correspondence. **b.** Cumulative distribution for the ratio of LT_{nuc} computed with the deposition function of Sharon & Kushnir to LT_{nuc} reported in this work. Shaded regions represent 68% confidence intervals computed by bootstrap resampling (10,000 samples). Vertical dashed blue, green, and red lines indicate mean values for SNe IIb, Ib, and Ic, respectively

Extended Data Table 1 SN sample.

SN	Type	cz (km s ⁻¹)	μ (mag)	E(B - V) _{IS} (mag)	E(B - V) _h (mag)	$M_{L,peak}$ (mag)	$t_{non-det}$ (MJD)	$t_{detected}$ (MJD)	t_{exp} (MJD)	Filters
1993J	IIb	-34	27.86 ± 0.05	0.069 ± 0.011	0.065 ± 0.074	-17.482	49,072.900	49,074.860	49,073.9 ± 0.6	BVRI
1994I	Ic	463	29.67 ± 0.07	0.031 ± 0.005	0.233 ± 0.092	-17.711	49,439.000	49,444.170	49,441.8 ± 1.4	BVRI
1996cb	IIb	713	30.48 ± 0.27	0.026 ± 0.004	-0.045 ± 0.074	-16.593	50,427.000	50,432.707	50,430.4 ± 1.5	BVRI
1998bw	Ic	2,599	32.60 ± 0.21	0.049 ± 0.008	-0.092 ± 0.065	-18.569	50,928.909	50,928.909	50,928.9 ± 0.0	BVRI
2003jd	Ic	5,654	34.30 ± 0.15	0.038 ± 0.006	0.070 ± 0.092	-18.614	52,928.000	52,937.000	52,931.3 ± 2.0	BVRI
2004gq	Ib	1,939	32.08 ± 0.19	0.063 ± 0.010	0.256 ± 0.084	-17.541	53,343.380	53,350.360	53,346.4 ± 1.8	BV gri
2005az	Ic	2,535	32.92 ± 0.19	0.010 ± 0.002	0.403 ± 0.083	-18.184	53,449.230	53,456.410	53,455.0 ± 1.2	V ri
2005hg	Ib	6,388	34.66 ± 0.12	0.089 ± 0.014	0.165 ± 0.095	-17.796	53,663.240	53,668.270	53,665.9 ± 1.4	BV ri
2006T	IIb	2,582	32.78 ± 0.19	0.064 ± 0.010	0.242 ± 0.115	-17.921	53,751.955	53,765.988	53,760.8 ± 2.9	BV gri
2006el	Ib	5,150	34.09 ± 0.14	0.098 ± 0.016	0.040 ± 0.079	-16.927	53,965.320	53,972.280	53,967.7 ± 1.7	BVR ri
2006ep	Ib	4,537	33.70 ± 0.16	0.031 ± 0.005	0.260 ± 0.065	-17.131	53,973.640	53,977.350	53,975.2 ± 1.0	BV gri
2006fo	Ib	6,205	34.56 ± 0.12	0.023 ± 0.004	0.300 ± 0.087	-17.904	53,975.410	53,994.430	53,987.8 ± 3.0	BV gri
2007gr	Ic	518	30.04 ± 0.19	0.053 ± 0.009	0.066 ± 0.063	-17.534	54,322.710	54,325.671	54,324.3 ± 0.8	BVRI ri
2007ru	Ic	4,636	33.78 ± 0.16	0.222 ± 0.035	0.067 ± 0.063	-18.848	54,426.160	54,431.900	54,428.5 ± 1.5	BVRI ri
2007uy	Ib	1,947	32.41 ± 0.19	0.019 ± 0.003	0.191 ± 0.065	-17.314	54,442.000	54,465.669	54,463.0 ± 2.0	BV ri
2008D	Ib	1,947	32.41 ± 0.19	0.019 ± 0.003	0.633 ± 0.089	-16.830	54,474.450	54,474.564	54,474.5 ± 0.0	BV ri
2008ax	IIb	565	29.54 ± 0.21	0.019 ± 0.003	0.268 ± 0.115	-16.770	54,528.190	54,528.450	54,528.3 ± 0.1	BVRI ri
2009bb	Ic	2,961	33.04 ± 0.18	0.085 ± 0.014	0.406 ± 0.085	-18.667	54,909.200	54,911.110	54,910.2 ± 0.5	BVRI gri
2009iz	Ib	4,256	33.60 ± 0.17	0.073 ± 0.012	0.053 ± 0.066	-17.016	55,081.450	55,093.520	55,089.4 ± 2.5	BV ri
2009if	Ib	2,381	32.37 ± 0.11	0.097 ± 0.016	-0.005 ± 0.064	-17.590	55,098.010	55,100.000	55,099.1 ± 0.6	BVRI gri
2010as	IIb	2,236	32.18 ± 0.24	0.147 ± 0.024	0.290 ± 0.114	-17.696	55,267.330	55,274.220	55,270.4 ± 1.8	BVRI gri
2011dh	IIb	463	29.67 ± 0.07	0.031 ± 0.005	0.145 ± 0.073	-17.616	55,712.275	55,712.893	55,712.6 ± 0.2	BVRI gri
PTF11klg	Ic	7,983	35.10 ± 0.10	0.075 ± 0.012	0.190 ± 0.125	-17.791	-	55,792.370	55,790.9 ± 1.2	gr
PTF12gzk	Ic	4,128	33.55 ± 0.20	0.043 ± 0.007	0.033 ± 0.063	-18.463	56,127.000	56,132.300	56,129.7 ± 1.4	gr
2013ge	Ic	1,306	31.78 ± 0.14	0.020 ± 0.003	0.193 ± 0.063	-17.721	56,597.788	56,604.796	56,603.0 ± 1.4	BVR r
iPTF13bvn	Ib	1,359	31.47 ± 0.19	0.044 ± 0.007	0.128 ± 0.063	-16.711	56,458.290	56,459.240	56,458.8 ± 0.3	BVRI gri
2014L	Ic	2,407	30.71 ± 0.40	0.033 ± 0.005	0.607 ± 0.092	-17.999	56,659.000	56,681.847	56,680.2 ± 1.4	BVRI
2014ad	Ic	1,716	32.10 ± 0.18	0.038 ± 0.006	-0.018 ± 0.067	-18.276	56,722.370	56,728.400	56,725.9 ± 1.6	BVRI
2015ap	Ib	3,410	33.12 ± 0.21	0.036 ± 0.006	0.056 ± 0.064	-18.102	-	57,273.000	57,269.1 ± 2.5	BVR gri
2016P	Ic	4,382	33.98 ± 0.17	0.023 ± 0.004	0.318 ± 0.085	-18.632	57,100.060	57,406.192	57,403.3 ± 1.9	BVRI gri
2016bau	Ib	1,156	31.67 ± 0.17	0.014 ± 0.002	0.262 ± 0.098	-17.079	57,451.998	57,460.974	57,459.1 ± 1.6	BVR
2016coi	Ic	1,093	30.90 ± 0.15	0.074 ± 0.012	0.074 ± 0.063	-17.812	57,529.540	57,535.550	57,533.0 ± 1.6	BVRI gri
2016gkg	IIb	1,481	31.23 ± 0.26	0.017 ± 0.003	0.109 ± 0.073	-16.607	57,651.197	57,651.234	57,651.2 ± 0.0	BVRI gri
2016iae	Ic	1,040	30.55 ± 0.17	0.013 ± 0.002	0.590 ± 0.086	-17.752	57,691.540	57,699.474	57,697.4 ± 1.6	BV ri
2016jdw	Ib	5,661	34.49 ± 0.12	0.010 ± 0.002	0.071 ± 0.073	-17.543	-	57,751.849	57,745.3 ± 3.0	gr
2017bgu	Ib	2,549	32.76 ± 0.19	0.018 ± 0.003	0.147 ± 0.072	-17.336	57,798.630	57,806.622	57,801.2 ± 1.8	gr
2017gpn	IIb	2,215	32.38 ± 0.19	0.293 ± 0.047	-0.018 ± 0.115	-17.059	57,982.620	57,988.620	57,985.0 ± 1.6	BVR gri
2018ie	Ic	4,267	33.88 ± 0.16	0.058 ± 0.009	0.090 ± 0.090	-17.676	58,130.530	58,132.590	58,131.5 ± 0.6	BV gri
2018dgg	Ic	7,590	35.07 ± 0.11	0.034 ± 0.005	0.260 ± 0.135	-17.978	58,302.330	58,305.309	58,303.8 ± 0.8	gr _{ZTF}
2019odp	Ic	4,303	33.65 ± 0.18	0.165 ± 0.026	-0.041 ± 0.117	-17.739	58,712.477	58,716.389	58,715.3 ± 0.9	gr _{ZTF}
2019ply	IIb	6,499	34.67 ± 0.13	0.125 ± 0.020	0.065 ± 0.128	-17.211	58,726.458	58,732.439	58,729.9 ± 1.6	gr _{ZTF}
2020oi	Ic	1,571	31.18 ± 0.05	0.023 ± 0.004	0.176 ± 0.068	-18.019	58,852.546	58,855.542	58,854.4 ± 0.8	BV gri gr _{ZTF}
2020bcq	Ib	5,545	34.48 ± 0.14	0.012 ± 0.002	0.027 ± 0.133	-17.505	58,871.540	58,875.475	58,873.7 ± 1.1	gr _{ZTF}
2020bvc	Ic	7,565	35.11 ± 0.10	0.011 ± 0.002	0.014 ± 0.066	-18.845	58,881.557	58,883.340	58,882.5 ± 0.5	BV gr gr _{ZTF}
2020hqn	Ic	7,566	35.14 ± 0.11	0.024 ± 0.004	0.097 ± 0.118	-17.704	58,954.458	58,956.319	58,955.4 ± 0.5	gr _{ZTF}
2020sai	Ib	8,596	35.32 ± 0.10	0.208 ± 0.033	0.013 ± 0.113	-17.629	59,079.449	59,082.451	59,080.8 ± 0.8	gr _{ZTF}
2020scb	Ic	5,225	34.10 ± 0.13	0.049 ± 0.008	0.245 ± 0.114	-18.371	59,086.358	59,087.377	59,086.9 ± 0.3	gr _{ZTF}
2020yvt	IIb	2,997	33.20 ± 0.22	0.011 ± 0.002	0.043 ± 0.148	-17.204	59,155.492	59,157.490	59,156.4 ± 0.6	gr _{ZTF}
2020abqx	Ib	18,901	37.15 ± 0.06	0.011 ± 0.002	-0.054 ± 0.133	-18.835	59,184.448	59,186.535	59,185.4 ± 0.6	gr _{ZTF}
2020acat	IIb	2,378	32.77 ± 0.22	0.021 ± 0.003	-0.032 ± 0.132	-17.786	59,190.609	59,192.630	59,191.5 ± 0.6	gr _{ZTF}
2020adow	Ic	2,226	32.77 ± 0.17	0.031 ± 0.005	-0.025 ± 0.074	-18.027	59,207.493	59,209.410	59,208.4 ± 0.5	gr _{ZTF}
2021do	Ic	2,802	33.06 ± 0.20	0.022 ± 0.004	0.648 ± 0.125	-18.756	59,216.410	59,216.454	59,216.4 ± 0.0	gr _{ZTF}
2021dww	Ic	7,793	35.14 ± 0.10	0.033 ± 0.005	0.007 ± 0.119	-17.655	59,270.421	59,272.420	59,271.5 ± 0.6	gr _{ZTF}
2021mxx	Ic	2,893	32.77 ± 0.19	0.082 ± 0.013	0.181 ± 0.113	-17.517	59,353.435	59,356.390	59,354.8 ± 0.8	gr _{ZTF}

Uncertainties are 1 σ errors.

32 *Engines in stripped-envelope supernovae***Extended Data Table 2** SN parameters.

SN	$\log M_{\text{Ni}} [M_{\odot}]$ (dex)	t_{esc} (d)	t_{peak} (d)	$\log L_{\text{peak}} [10^{43} \text{ erg s}^{-1}]$ (dex)	Δm_{15} (mag)	V_{peak} (km s^{-1})
1993J	-1.129 ± 0.070	109 ⁺² ₋₂	20.9 ± 0.6	-0.601 ± 0.080	0.880 ± 0.010	7,000 ± 1,050
1994I	-1.729 ± 0.126	112 ⁺³ ₋₃	9.6 ± 1.4	-0.589 ± 0.131	1.478 ± 0.020	9,000 ± 1,350
1996cb	-1.344 ± 0.126	94 ⁺¹ ₋₁	21.0 ± 1.5	-0.943 ± 0.135	0.727 ± 0.007	7,000 ± 1,050
1998bw	-0.856 ± 0.122	116 ⁺¹ ₋₁	16.0 ± 0.4	-0.235 ± 0.127	0.615 ± 0.018	15,000 ± 2,250
2003jd	-0.937 ± 0.137	86 ⁺³ ₋₃	13.0 ± 2.0	-0.182 ± 0.148	0.807 ± 0.010	13,000 ± 1,950
2004gq	-1.116 ± 0.105	104 ⁺¹ ₋₁	13.0 ± 1.8	-0.503 ± 0.126	0.762 ± 0.010	12,000 ± 1,800
2005az	-0.838 ± 0.123	125 ⁺⁵ ₋₄	20.2 ± 1.3	-0.398 ± 0.142	0.345 ± 0.018	11,000 ± 1,650
2005hg	-0.992 ± 0.101	116 ⁺⁴ ₋₄	17.2 ± 1.4	-0.455 ± 0.120	0.562 ± 0.007	7,000 ± 1,050
2006T	-1.014 ± 0.120	110 ⁺¹ ₋₁	19.2 ± 2.9	-0.433 ± 0.147	0.792 ± 0.005	6,000 ± 900
2006el	-1.354 ± 0.088	112 ⁺⁵ ₋₄	15.9 ± 1.7	-0.830 ± 0.102	0.640 ± 0.013	8,000 ± 1,200
2006ep	-1.378 ± 0.086	101 ⁺³ ₋₃	11.9 ± 1.0	-0.731 ± 0.097	0.655 ± 0.005	7,000 ± 1,050
2006fo	-0.858 ± 0.089	129 ⁺⁴ ₋₃	15.7 ± 3.0	-0.402 ± 0.116	0.500 ± 0.013	5,500 ± 825
2007gr	-1.382 ± 0.112	147 ⁺³ ₋₃	14.7 ± 0.9	-0.662 ± 0.117	0.695 ± 0.005	7,000 ± 1,050
2007ru	-1.004 ± 0.109	92 ⁺¹ ₋₁	10.4 ± 1.5	-0.145 ± 0.121	0.688 ± 0.010	19,000 ± 2,850
2007uy	-1.233 ± 0.096	100 ⁺¹ ₋₁	18.1 ± 2.0	-0.707 ± 0.102	0.587 ± 0.007	15,000 ± 2,250
2008D	-1.327 ± 0.108	100 ⁺² ₋₂	19.0 ± 0.1	-0.854 ± 0.120	0.583 ± 0.007	8,000 ± 1,200
2008ax	-1.392 ± 0.129	102 ⁺¹ ₋₁	20.8 ± 0.1	-0.841 ± 0.152	0.850 ± 0.022	6,000 ± 900
2009bb	-0.941 ± 0.139	71 ⁺⁸ ₋₉	12.3 ± 0.5	-0.169 ± 0.152	1.015 ± 0.007	20,000 ± 3,000
2009iz	-1.145 ± 0.091	117 ⁺⁸ ₋₅	18.8 ± 2.5	-0.774 ± 0.104	0.388 ± 0.007	5,000 ± 750
2009jf	-0.994 ± 0.072	121 ⁺¹ ₋₁	22.0 ± 0.6	-0.534 ± 0.084	0.490 ± 0.003	7,000 ± 1,050
2010as	-1.081 ± 0.134	110 ⁺⁴ ₋₄	17.2 ± 1.8	-0.505 ± 0.159	0.670 ± 0.005	6,000 ± 900
2011dh	-1.103 ± 0.067	106 ⁺² ₋₂	20.2 ± 0.3	-0.572 ± 0.081	0.795 ± 0.007	7,000 ± 1,050
PTF11klg	-1.151 ± 0.168	151 ⁺⁷ ₋₅	14.4 ± 1.2	-0.504 ± 0.222	0.858 ± 0.015	8,172 ± 1,226
PTF12gzk	-0.762 ± 0.115	106 ⁺² ₋₂	18.3 ± 1.4	-0.310 ± 0.122	0.357 ± 0.010	16,000 ± 2,400
2013ge	-1.165 ± 0.101	171 ⁺³ ₋₃	17.2 ± 1.5	-0.561 ± 0.112	0.585 ± 0.015	9,000 ± 1,350
iPTF13bvn	-1.582 ± 0.095	103 ⁺⁵ ₋₄	16.5 ± 0.3	-0.901 ± 0.104	0.988 ± 0.020	6,000 ± 900
2014L	-1.164 ± 0.201	120 ⁺² ₋₂	14.4 ± 1.4	-0.448 ± 0.213	0.905 ± 0.010	7,800 ± 1,170
2014ad	-1.045 ± 0.114	96 ⁺¹ ₋₁	14.3 ± 1.6	-0.391 ± 0.115	0.737 ± 0.005	22,300 ± 3,345
2015ap	-0.966 ± 0.102	89 ⁺¹ ₋₁	15.6 ± 2.5	-0.302 ± 0.115	0.843 ± 0.007	9,000 ± 1,350
2016P	-0.934 ± 0.129	104 ⁺⁸ ₋₈	12.0 ± 1.9	-0.190 ± 0.147	0.885 ± 0.007	7,000 ± 1,050
2016bau	-1.373 ± 0.117	117 ⁺¹¹ ₋₉	18.4 ± 1.6	-0.766 ± 0.124	0.797 ± 0.025	–
2016coi	-1.180 ± 0.097	158 ⁺² ₋₂	17.7 ± 1.6	-0.618 ± 0.111	0.455 ± 0.005	15,000 ± 2,250
2016gkg	-1.464 ± 0.120	119 ⁺² ₋₂	19.8 ± 0.1	-0.933 ± 0.134	0.890 ± 0.007	8,000 ± 1,200
2016iae	-1.236 ± 0.123	120 ⁺² ₋₂	13.6 ± 1.6	-0.532 ± 0.152	0.673 ± 0.010	9,000 ± 1,350
2016jdw	-1.057 ± 0.086	121 ⁺¹¹ ₋₇	18.0 ± 3.0	-0.589 ± 0.097	0.510 ± 0.020	11,000 ± 1,650
2017bgu	-1.138 ± 0.101	–	16.9 ± 1.8	-0.696 ± 0.108	0.445 ± 0.013	8,500 ± 1,275
2017gpn	-1.251 ± 0.127	81 ⁺¹ ₋₁	16.2 ± 1.6	-0.710 ± 0.162	0.858 ± 0.015	8,000 ± 1,200
2018ie	-1.589 ± 0.133	113 ⁺¹³ ₋₇	7.6 ± 0.6	-0.524 ± 0.160	1.315 ± 0.018	23,000 ± 3,450
2018dgx	-0.962 ± 0.184	–	12.2 ± 0.9	-0.432 ± 0.240	0.503 ± 0.035	8,670 ± 1,300
2019ocdp	-1.046 ± 0.174	119 ⁺⁶ ₋₅	19.6 ± 0.9	-0.606 ± 0.207	0.522 ± 0.013	–
2019ply	-1.259 ± 0.129	–	21.5 ± 1.6	-0.691 ± 0.165	0.730 ± 0.043	–
2020oi	-1.562 ± 0.087	80 ⁺⁵ ₋₅	10.7 ± 0.9	-0.417 ± 0.111	1.680 ± 0.040	12,750 ± 1,912
2020bcq	-1.454 ± 0.140	–	13.7 ± 1.1	-0.574 ± 0.175	1.052 ± 0.083	–
2020bvc	-0.691 ± 0.124	63 ⁺⁶ ₋₉	13.3 ± 0.5	-0.150 ± 0.112	0.655 ± 0.018	20,900 ± 3,135
2020hqn	-1.112 ± 0.174	100 ⁺²³⁰ ₋₁₃	16.7 ± 0.5	-0.622 ± 0.193	0.508 ± 0.025	6,000 ± 900
2020sai	-1.112 ± 0.122	–	15.2 ± 0.9	-0.540 ± 0.152	0.568 ± 0.030	–
2020scb	-0.982 ± 0.171	94 ⁺¹⁸ ₋₁₃	12.1 ± 0.5	-0.289 ± 0.203	0.850 ± 0.035	12,500 ± 1,875
2020yvt	-1.333 ± 0.158	120 ⁺¹⁴ ₋₈	14.6 ± 0.6	-0.717 ± 0.196	0.717 ± 0.025	–
2020abqx	-0.512 ± 0.130	–	17.6 ± 0.7	-0.126 ± 0.146	0.438 ± 0.048	–
2020acat	-1.060 ± 0.146	125 ⁺⁵ ₋₄	16.1 ± 0.6	-0.506 ± 0.171	0.683 ± 0.027	10,000 ± 1,500
2020adow	-1.350 ± 0.124	94 ⁺⁵ ₋₅	9.0 ± 0.5	-0.425 ± 0.141	1.087 ± 0.022	–
2021do	-0.988 ± 0.193	87 ⁺¹¹ ₋₁₀	9.7 ± 0.2	-0.111 ± 0.234	1.083 ± 0.035	–
2021dwg	-1.109 ± 0.166	105 ⁺¹⁵ ₋₁₀	17.9 ± 0.8	-0.635 ± 0.186	0.493 ± 0.027	–
2021mxx	-1.574 ± 0.171	–	9.8 ± 0.9	-0.676 ± 0.200	1.005 ± 0.048	9,500 ± 1,425

Uncertainties are 1σ errors, while lower and upper t_{esc} errors are 16th and 84th percentiles.

Extended Data Table 3 $LT_{\text{-nuc}}$ and $LT_{\text{-nuc}}/LT_{100}$ values.

SN	$LT_{\text{-nuc}}$ (10^{54} erg s)	$LT_{\text{-nuc}}/LT_{100}$	SN	$LT_{\text{-nuc}}$ (10^{54} erg s)	$LT_{\text{-nuc}}/LT_{100}$
1993J	$2.37^{+0.67}_{-0.52}$	0.094 ± 0.011	2014ad	$5.94^{+1.93}_{-1.46}$	0.182 ± 0.015
1994I	$3.17^{+1.15}_{-0.84}$	0.353 ± 0.026	2015ap	$6.92^{+2.87}_{-2.03}$	0.184 ± 0.028
1996cb	$0.18^{+0.38}_{-0.12}$	0.013 ± 0.013	2016P	$8.29^{+4.62}_{-2.97}$	0.194 ± 0.038
1998bw	$12.27^{+4.17}_{-3.11}$	0.220 ± 0.005	2016bau	$2.74^{+1.23}_{-0.85}$	0.172 ± 0.035
2003jd	$10.21^{+4.22}_{-2.99}$	0.239 ± 0.026	2016coi	$7.14^{+2.49}_{-1.85}$	0.246 ± 0.023
2004gq	$2.64^{+1.02}_{-0.74}$	0.102 ± 0.012	2016gkg	$1.16^{+0.69}_{-0.43}$	0.097 ± 0.023
2005az	$6.77^{+3.58}_{-2.34}$	0.127 ± 0.022	2016iae	$5.42^{+3.24}_{-2.03}$	0.228 ± 0.041
2005hg	$5.15^{+2.73}_{-1.79}$	0.139 ± 0.029	2016jdw	$2.85^{+1.67}_{-1.05}$	0.093 ± 0.028
2006T	$4.66^{+2.99}_{-1.82}$	0.134 ± 0.031	2017bgu	$2.16^{+0.99}_{-0.68}$	0.081 ± 0.015
2006el	$1.57^{+0.61}_{-0.44}$	0.102 ± 0.019	2017gpn	$1.30^{+1.00}_{-0.57}$	0.078 ± 0.023
2006ep	$1.87^{+0.50}_{-0.39}$	0.129 ± 0.012	2018ie	$2.98^{+1.31}_{-0.91}$	0.270 ± 0.021
2006fo	$4.06^{+2.53}_{-1.56}$	0.083 ± 0.023	2018dgx	$4.39^{+4.46}_{-2.21}$	0.107 ± 0.033
2007gr	$4.89^{+1.48}_{-1.14}$	0.263 ± 0.013	2019odp	$3.44^{+2.88}_{-1.57}$	0.108 ± 0.026
2007ru	$14.21^{+4.50}_{-3.42}$	0.331 ± 0.026	2019ply	$3.13^{+2.40}_{-1.36}$	0.144 ± 0.063
2007uy	$3.07^{+1.12}_{-0.82}$	0.149 ± 0.020	2020oi	$4.70^{+1.34}_{-1.04}$	0.388 ± 0.026
2008D	$1.57^{+0.88}_{-0.56}$	0.100 ± 0.023	2020bcq	$4.21^{+2.17}_{-1.43}$	0.263 ± 0.040
2008ax	$1.65^{+0.99}_{-0.62}$	0.118 ± 0.022	2020bvc	$5.80^{+5.89}_{-2.92}$	0.108 ± 0.068
2009bb	$7.31^{+3.82}_{-2.51}$	0.200 ± 0.046	2020hqn	$2.07^{+3.08}_{-1.24}$	0.082 ± 0.060
2009iz	$1.07^{+0.80}_{-0.46}$	0.045 ± 0.018	2020sai	$4.23^{+1.91}_{-1.32}$	0.140 ± 0.030
2009jf	$4.71^{+1.41}_{-1.08}$	0.128 ± 0.013	2020scb	$6.04^{+4.71}_{-2.65}$	0.165 ± 0.059
2010as	$5.13^{+4.29}_{-2.34}$	0.169 ± 0.051	2020yvt	$1.70^{+1.35}_{-0.75}$	0.103 ± 0.032
2011dh	$2.95^{+0.89}_{-0.68}$	0.109 ± 0.012	2020abqx	$4.49^{+7.66}_{-2.83}$	0.042 ± 0.036
PTF11klg	$3.06^{+3.95}_{-1.72}$	0.115 ± 0.051	2020acat	$3.11^{+1.43}_{-0.98}$	0.100 ± 0.013
PTF12gzk	$8.51^{+3.23}_{-2.34}$	0.138 ± 0.013	2020adow	$4.40^{+1.58}_{-1.16}$	0.252 ± 0.018
2013ge	$8.10^{+2.67}_{-2.01}$	0.262 ± 0.021	2021do	$9.01^{+6.78}_{-3.87}$	0.236 ± 0.051
iPTF13bvn	$1.86^{+0.56}_{-0.43}$	0.190 ± 0.016	2021dwg	$3.28^{+2.91}_{-1.54}$	0.121 ± 0.044
2014L	$4.76^{+3.02}_{-1.85}$	0.181 ± 0.014	2021mxx	$3.15^{+1.86}_{-1.17}$	0.260 ± 0.041

Lower and upper $LT_{\text{-nuc}}$ errors are 16th and 84th percentiles, while $LT_{\text{-nuc}}/LT_{100}$ uncertainties are 1σ errors.